The Effect of Galaxy Interactions on Molecular Gas Properties

Hsi-An Pan[1], Lihwai Lin[1], Bau-Ching Hsieh[1], Ting Xiao[2,3], Yang Gao[3], Sara L. Ellison[4], Jillian M. Scudder[5], Jorge Barrera-Ballesteros[6], Fangting Yuan[3], Amélie Saintonge[7], Christine D. Wilson[8], Ho Seong Hwang[9], Ilse De Looze[7,10], Yu Gao[11], Luis C. Ho[12,13], Elias Brinks[14], Angus Mok[15], Toby Brown[8], Timothy A. Davis[16], Thomas G. Williams[16], Aeree Chung[17], Harriet Parsons[18], Martin Bureau[19], Mark T. Sargent[20], Eun Jung Chung[21], Eunbin Kim[21,22], Tie Liu[18,21,23], Michał J. Michałowski[24], and Tomoka Tosaki[25]

[1] Institute of Astronomy and Astrophysics, Academia Sinica, AS/NTU Astronomy-Mathematics Building, No. 1, Section 4, Roosevelt Rd., Taipei 10617, Taiwan
hapan@asiaa.sinica.edu.tw

[2] Department of Physics, Zhejiang University, Hangzhou 310027, People's Republic of China

[3] Shanghai Astronomical Observatory, Nandan Road 80, Shanghai 200030, People's Republic of China

[4] Department of Physics and Astronomy, University of Victoria, Finnerty Road, Victoria, BC V8P 1A1, Canada

[5] Department of Physics and Astronomy, Oberlin College, Oberlin, OH 44074, USA

[6] Department of Physics and Astronomy, Johns Hopkins University, Bloomberg Center, 3400 N. Charles St., Baltimore, MD 21218, USA

[7] University College London, Gower Street, London WC1E 6BT, UK

[8] Department of Physics and Astronomy, McMaster University, Hamilton, ON L8S 4M1, Canada

[9] Quantum Universe Center, Korea Institute for Advanced Study, 85 Hoegiro, Dongdaemun-gu, Seoul 02455, Republic of Korea

[10] Sterrenkundig Observatorium, Ghent University, Krijgslaan 281—S9, B-9000 Ghent, Belgium

[11] Purple Mountain Observatory & Key Laboratory for Radio Astronomy, Chinese Academy of Sciences, 8 Yuanhua Road, Nanjing 210034, People's Republic of China

[12] Kavli Institute for Astronomy and Astrophysics, Peking University, Beijing 100871, People's Republic of China

[13] Department of Astronomy, School of Physics, Peking University, Beijing 100871, People's Republic of China

[14] Centre for Astrophysics Research, University of Hertfordshire, College Lane, Hatfield AL10 9AB, UK

[15] Department of Physics & Astronomy, University of Toledo, Toledo, OH 43606, USA

[16] School of Physics and Astronomy, Cardiff University, Queen's Building, The Parade, Cardiff CF24 3AA, UK

[17] Department of Astronomy, Yonsei University, 50 Yonsei-ro, Seodaemun-gu, Seoul 03722, Republic of Korea

[18] East Asian Observatory, 660 N. A'ohoku Place, Hilo, HI 96720, USA

[19] Sub-Department of Astrophysics, University of Oxford, Denys Wilkinson Building, Keble Road, Oxford OX1 3RH, UK

[20] Astronomy Centre, Department of Physics and Astronomy, University of Sussex, Brighton BN1 9QH, UK

[21] Korea Astronomy and Space Science Institute, 776 Daedeokdaero, Yuseong-gu, Daejeon 34055, Republic of Korea

[22] School of Space Research, Kyung Hee University, Yongin, Gyeonggi 17104, Republic of Korea

[23] National Astronomical Observatories, Chinese Academy of Sciences, A20 Datun Road, Chaoyang District, Beijing 100012, People's Republic of China

[24] Astronomical Observatory Institute, Faculty of Physics, Adam Mickiewicz University, ul. Słoneczna 36, 60-286 Poznaó, Poland

[25] Joetsu University of Education, Yamayashiki-machi, Joetsu, Niigata 943-8512, Japan

Abstract

Galaxy interactions are often accompanied by an enhanced star formation rate (SFR). Since molecular gas is essential for star formation, it is vital to establish whether and by how much galaxy interactions affect the molecular gas properties. We investigate the effect of interactions on global molecular gas properties by studying a sample of 58 galaxies in pairs and 154 control galaxies. Molecular gas properties are determined from observations with the JCMT, PMO, and CSO telescopes and supplemented with data from the xCOLD GASS and JINGLE surveys at $^{12}CO(1–0)$ and $^{12}CO(2–1)$. The SFR, gas mass (M_{H_2}), and gas fraction (f_{gas}) are all enhanced in galaxies in pairs by $\sim$2.5 times compared to the controls matched in redshift, mass, and effective radius, while the enhancement of star formation efficiency (SFE $\equiv$ SFR/M_{H_2}) is less than a factor of 2. We also find that the enhancements in SFR, M_{H_2} and f_{gas}, increase with decreasing pair separation and are larger in systems with smaller stellar mass ratio. Conversely, the SFE is only enhanced in close pairs (separation $<$20 kpc) and equal-mass systems; therefore, most galaxies in pairs lie in the same parameter space on the SFR–M_{H_2} plane as controls. This is the first time that the dependence of molecular gas properties on merger configurations is probed statistically with a relatively large sample and a carefully selected control sample for individual galaxies. We conclude that galaxy interactions do modify the molecular gas properties, although the strength of the effect is dependent on merger configuration.

Key words: galaxies: interactions – galaxies: ISM – ISM: molecules – galaxies: star formation

1. Introduction

It has been well established that galaxy interactions can trigger bursts of star formation. Interaction-triggered star formation was first observed by Larson & Tinsley (1978), who found that interacting galaxies have large dispersion in $U - B/B - V$ colors due to the short-duration starbursts. Since then, many observations have confirmed this finding (e.g., Darg et al. 2010a; Scudder et al. 2012; Knapen et al. 2015). Observationally, the strongest starbursts (e.g., ultraluminous infrared galaxies (ULIRGs)) are predominantly merging

systems (Sanders et al. 1988; Borne et al. 1999), which supports the idea that galaxy interactions are efficient in converting gas to stars. Simulations also show that external perturbations can trigger star formation by the gas inflow induced as a result of tidal forces (e.g., Barnes & Hernquist 1996; Di Matteo et al. 2007; Moreno et al. 2015).

However, an enhanced star formation rate (SFR) is not ubiquitous in interacting galaxies. The average level of the SFR enhancement of galaxy pairs, as measured in both observations and simulations, is moderate, typically below a factor of a few

(Di Matteo et al. 2007, 2008; Lin et al. 2007; Martig & Bournaud 2008; Hwang et al. 2011; Wong et al. 2011; Scudder et al. 2012; Xu et al. 2012; Ellison et al. 2013; Knapen et al. 2015). Star formation enhancement depends on parameters such as separation between galaxies in pairs (Lambas et al. 2003; Ellison et al. 2008; Park & Choi 2009; Hwang et al. 2010; Scudder et al. 2012; Patton et al. 2013; Davies et al. 2015), the properties of the progenitor galaxies (Mihos & Hernquist 1996; Cox et al. 2008; Xu et al. 2010; Scudder et al. 2012; Davies et al. 2015), merging geometry (Springel & Hernquist 2005; Di Matteo et al. 2007; Moreno et al. 2015; Sparre & Springel 2016), and gas (H I) fraction (Scudder et al. 2015).

Given that SFR depends on the molecular gas reservoir (Kennicutt 1998a), one would expect that the amount or physical properties of the molecular gas change while a galaxy undergoes an interaction with another galaxy (e.g., Moreno et al. 2018). Two possibilities for enhanced star formation in galaxy pairs are most commonly proposed: (1) an enrichment of the molecular gas reservoir, which fuels star formation (e.g., Combes et al. 1994; Casasola et al. 2004), and (2) an increase in the efficiency of converting gas into stars (e.g., Solomon & Sage 1988; Sofue et al. 1993; Michiyama et al. 2016). Both scenarios have observationally testable predictions—the former predicts higher molecular gas mass (M_{H_2}), or, more precisely, a higher molecular gas mass fraction with respect to the total (gas and stars) mass (f_{gas}), while the latter predicts a higher star formation efficiency (SFE) of molecular gas.

However, observations of H_2 in interacting galaxies have yet to give a clear picture of whether it is the total gas reservoir or the SFE that drives the enhanced SFR in galaxy pairs. Solomon & Sage (1988) observed $^{12}CO(1–0)$ in 93 far-infrared-bright pairs and classified them into five types according to the degree of interaction. They found that there is no significant difference in CO luminosity (given that $L_{CO} \propto M_{H_2}$) between their pair types and isolated galaxies. On the other hand, strong interactions give rise to an increase in L_{FIR}/L_{CO} ratio ($\propto$SFE). Sofue et al. (1993) also found an elevated SFE in their 54 interacting galaxies taken from the Arp Atlas. More recently, Michiyama et al. (2016) revealed an increasing SFE from isolated to interacting galaxies and from early-stage to late-stage interactions using a sample of 60 interacting and 28 isolated galaxies.[26] Yet several studies have arrived at the opposite conclusion. For example, Combes et al. (1994) observed $^{12}CO(1–0)$ in 51 interacting galaxies and found that the total molecular content increases with decreasing projected separation of the pairs, while SFE does not. Accordingly, they concluded that the total molecular content plays a more significant role in triggering star formation than SFE. A similar result is also reached by Casasola et al. (2004) using several hundred interacting galaxies and ~2000 normal galaxies compiled from the literature.

Although the above results indicate that galaxy interactions may affect the molecular gas properties, the above analyses have several shortcomings that might contribute to their conflicting results. For example, the global properties of the control galaxies to be compared with pairs should be carefully controlled. The majority of previous studies compare the properties of interacting and isolated galaxies directly, where the latter may not always be the perfect reference in terms of the distributions of their redshift, stellar mass (M_*), and other galaxy properties.

Another important factor is the choice of CO-to-H_2 conversion factor (α_{CO}) between the measured L_{CO} and M_{H_2}. The validity of the widely adopted Galactic α_{CO} is often questioned (see the review by Bolatto et al. 2013). Empirically, α_{CO} increases with decreasing gas-phase metallicity 12+log(O/H) due to the decreasing abundance of CO relative to H_2 (Arimoto et al. 1996; Leroy et al. 2011; Narayanan et al. 2012). Since gas-phase metallicity is known to correlate with the M_*, M_{H_2}, and SFR of a galaxy (Tremonti et al. 2004; Mannucci et al. 2010; Bothwell et al. 2016), a physically motivated α_{CO} is essential for the study of molecular gas in galaxies.

Recently, Violino et al. (2018) took a step toward addressing these improvements by considering a control sample with properties matched to the galaxy pairs and using a physically motivated α_{CO}. They found that galaxy pairs have higher SFE and f_{gas} compared to the control sample. However, the investigation of the relation between merger configuration and gas properties is limited by the small sample size (11 galaxies in pairs) in Violino et al. (2018). It remains untested about how the change in gas properties correlates with the details of galaxy interaction properties, such as pair separation and mass ratio.

In this paper, we study molecular gas properties, which are calculated using a physically motivated value of α_{CO}, toward a sample of 58 galaxies in pairs. We compare their star formation and molecular gas properties with a sample of carefully matched control galaxies. The sample uniquely covers major and minor mergers (from equal-mass merger to a ratio of ~100), widely separated pairs and close pairs, and primary (higher M_*) and secondary (lower M_*) galaxies in a pair. This is the first time that the dependence of molecular gas properties on merger properties is probed statistically with a relatively large sample and carefully selected control sample for individual galaxies in pairs.

This paper is organized as follows. In Section 2, we describe our pair identification and data used in the analysis. In Sections 3.1 and 3.2, we first compare the SFR and molecular gas properties of the galaxies in pairs and the control sample by comparing the medians of the two samples. Next, in Sections 3.3 and 3.4, we explore the dependence of SFR and gas properties on merger properties, including projected separation and the stellar mass ratio of the two galaxies in a pair. In Section 4, we discuss the potential driver of star formation in galaxies in pairs and the locus of our galaxies in the SFR–M_{H_2} relation. The main results are summarized in Section 5.

Throughout this paper, we assume $\Omega_m = 0.3$, $\Omega_\Lambda = 0.7$, $H_0 = 70\,km\,s^{-1}\,Mpc^{-1}$, and a Kroupa initial mass function (IMF) of stars (Kroupa 2001).

2. Data

2.1. Molecular Gas Observations of Galaxies in Pairs

The pair samples in this work are either obtained by our group or compiled from several surveys, summarized in Table 1. The final sample consists of 58 galaxies in pairs and 154 isolated galaxies from which the control galaxies are drawn. The galaxies in pairs we refer to here are galaxies with a spectroscopic or morphological companion. In most of the cases discussed in this paper, the molecular gas observations were made toward one of the galaxies in a pair, except a few close pairs. Emission from the companion might be detected

---

[26] But note that they use $^{12}CO(3–2)$ as a molecular gas tracer, which may not trace total gas content due to the high critical density of $^{12}CO(3–2)$ (a few times $10^3\,cm^{-3}$).

Table 1
Summary of the Observations

	Galaxies in Pairs				Pool of Controls
Project	PI programs	JINGLE	JINGLE Pilot	xCOLD GASS	xCOLD GASS
Number	21	5	2+2+1	27	154
Telescope	JCMT	JCMT	JCMT/PMO/CSO	IRAM	IRAM
Tracer	^{12}CO(2–1)	^{12}CO(2–1)	^{12}CO(2–1)/(1–0)/(2–1)	^{12}CO(1–0)	^{12}CO(1–0)
Beam size	22″	22″	22″/52″/30″	22″	22″

for the pairs with the smallest projected separations. The potential effect of this contamination will be discussed in Section 4.1. Details of the sample selection, observations, and data reduction are described in this section.

2.1.1. Pair Sample: JCMT Observations (PI Programs)

The molecular gas observations of about half of the galaxies in pairs were obtained through our two PI programs on the James Clerk Maxwell Telescope (JCMT; project codes: M17AP060 and M17BP053; PI: H.-A. Pan).

The pair sample was selected from the 2779 galaxies in the fifth product launch (MPL-5, corresponding to SDSS DR13) of Mapping Nearby Galaxies at APO (MaNGA). MaNGA is part of the fourth generation of the Sloan Digital Sky Survey (SDSS-IV; Gunn et al. 2006; Blanton et al. 2017) and aims to obtain spatially resolved spectroscopy of 10,000 galaxies with a median redshift of ∼0.03 by 2020. MaNGA has a wavelength coverage of 3600–10300 Å, with a spectral resolution varying from $R \sim 1400$ at 4000 Å to $R \sim 2600$ around 9000 Å. Further details of the science goals, as well as sample selection, can be found in Bundy et al. (2015) and Wake et al. (2017). While this work focuses on the globally integrated star formation and molecular gas properties, the existence of MaNGA data will be beneficial in advancing the analysis of the spatially resolved properties in the future.

We first identify galaxies in pairs in these 2779 MaNGA galaxies. The galaxies in pairs are defined as those systems with projected separation $(r_p) < 50 \, \mathrm{kpc \, h^{-1}}$ (around 71.4 kpc with $h = 0.7$) and line-of-sight velocity difference $(\Delta V) < 500 \, \mathrm{km \, s^{-1}}$ (e.g., Patton et al. 2002; Lin et al. 2004). It has been noticed that the SFR enhancement can extend out to 150 kpc (Patton et al. 2013), although the enhancement for $r_p > 100$ kpc is almost negligible. Moreover, even with spectroscopic redshifts, interlopers may still exist and become a more significant effect with larger separation. For these reasons, the criterion of 50 kpc h^{-1} seems to be a reasonable choice. These criteria identified 662 galaxies in pairs. However, if the two merger components are too close (normally late-stage mergers) to be deblended by SDSS or do not have two separate spectroscopic redshift measurements, they will not be identified as galaxies in pairs. To pick up those late-stage systems, we use the "P-merger" parameter (weighted-merger-vote fraction) from Galaxy Zoo (Darg et al. 2010a, 2010b). The P-merger parameter quantifies the probability that an object is a merger based on visual inspection of large numbers of objects by human classifiers. It ranges from 0, an object looks nothing like a merger, to 1, an object looks unmistakably so. The criteria of P-merger > 0.4 suggested by Darg et al. (2010a, 2010b) is applied to select galaxies in pairs. The number of galaxies in pairs in the MaNGA sample increases to 736 by adding the Galaxy Zoo criterion.

The required observing time for JCMT ^{12}CO(2–1) observations for each of the identified galaxies in pairs is estimated in the following way. We first calculate the expected M_{H_2} from the *Wide-field Infrared Survey Explorer* 12 μm luminosity ($L_{12 \, \mu m}$) using the $L_{12 \, \mu m}$–M_{H_2} relation proposed by Jiang et al. (2015). Since 12 μm emission is a good tracer of star formation (Donoso et al. 2012; Lee et al. 2013), the relation is essentially the same as the Kennicutt–Schmidt relation. The ^{12}CO(1–0) luminosity is calculated from M_{H_2} using the Milky Way value for α_{CO} of 4.3 $M_\odot$ (K km s^{-1} pc^2)$^{-1}$ (Bolatto et al. 2013). Subsequently, the luminosity and flux of ^{12}CO(2–1) is derived assuming a ^{12}CO(2–1) to ^{12}CO(1–0) line intensity ratio (R_{21}) of 0.6. The adopted R_{21} here is a conservative choice (lower limit) for time estimation, as R_{21} is found to be 0.6–1.0 in nearby galaxies (e.g., Braine & Combes 1992; Leroy et al. 2009). Although we made conservative assumptions for R_{21} and α_{CO} for the purpose of estimating the exposure time, later we will use a different R_{21} that is chosen based on gas properties; moreover, we will present a physically motivated α_{CO} prescription that computes the value on a galaxy-by-galaxy basis in Section 3.1 and explore these assumptions in Section 4.4. Finally, we estimate the required time for a 4σ detection with a velocity resolution of 30 km s^{-1} for each identified galaxy in pairs and propose to observe 41 galaxies that have a suitable declination range and require on-source time of <250 minutes each. Any possible bias introduced by this latter choice will be discussed in Section 4.1.

The ^{12}CO(2–1) (230.538 GHz) observations of the 41 galaxies in pairs were obtained by JCMT using the RxA3m receiver (but only 21 galaxies were used for the analysis after a further control on galaxy properties; we will show the criteria in the next paragraph). The redshift range of these galaxies in pairs is 0.02–0.06. The beam size of the telescope is 22″ at 230 GHz. The observations were conducted during several periods from 2016 November to 2018 January. The sky opacity at 225 GHz was reported by the JCMT's Water Vapour Monitor (WVM), an in-cabin line-of-sight radiometer assessing the 183 GHz water line (reported at 225 GHz for historic reasons). The typical sky opacity was 0.08–0.20. The typical system temperatures were between 200 and 400 K. The on-source time for individual galaxies ranged from 40 minutes to 4 hr. The total on-source time for the two PI programs was ∼90 hr. The data reduction was done using the Starlink software (Currie et al. 2014). Individual exposures (∼20–40 minutes, including calibration) of a given galaxy were calibrated separately and then coadded. The spectrum was binned to a velocity resolution of 30 km s^{-1}. A linear baseline was subtracted from the spectrum using line-free channels. For a few galaxies for which the baseline is structured, a second- or third-order polynomial was used to subtract the baseline. Spectra were converted from antenna temperature in K to Jy by applying a factor of 15.6/η_a, where the aperture efficiency η_a is 0.55. The integrated CO luminosity L_{CO} is computed following

Solomon et al. ([1997](#)),

$$\frac{L_{CO}}{(\text{K km s}^{-1} \text{ pc}^2)} = 3.27 \times 10^7 S_{CO} \nu_{CO}^{-2} D_L^2 (1+z)^{-3}. \quad (1)$$

In this expression, S_{CO} is the line flux in units of Jy km s^{-1}, ν_{CO} is the observed frequency in GHz, and D_L represents the luminosity distance in Mpc. For ^{12}CO (2–1) observations, a ^{12}CO (2–1)-to-^{12}CO(1–0) intensity ratio of 0.8 is assumed when calculating L_{CO} (Leroy et al. [2009](#)). If the gas is optically thick, a ratio of 0.8 corresponds to an excitation temperature of $\sim$10 K. A detection (i.e., signal-to-noise ratio (S/N) >3) rate of $\sim$90% is achieved, implying that the approach we have taken to calculate the required sensitivity is valid.

Although 41 galaxies in pairs were obtained from the PI programs, only 21 galaxies are used for the analysis in this paper. Since the control sample used in this work (Section [2.2](#)) has a stellar mass cut of $\log(M_*/M_\odot) = 9$ (Saintonge et al. [2017](#)), we remove galaxies that have M_* less than this value. Moreover, only spiral galaxies are used, because early-type galaxies potentially have lower SFR, M_{H_2}, and f_{gas}, which may be irrelevant to the existence of interaction or not. The Galaxy Zoo property, a debiased probability of being a spiral galaxy "P-CS," is used to identify galaxy morphology. We select galaxies that have P-CS $\geqslant$ 0.6. All of the 21 galaxies in pairs have a solid detection by JCMT. Of these, 20 are selected based on pair separation, and one is based on the Galaxy Zoo morphology.

2.1.2. Pair Sample: JINGLE

The JCMT dust and gas In Nearby Galaxies Legacy Exploration (JINGLE) is an ongoing JCMT Large Program (Saintonge et al. [2018](#)). JINGLE is designed to systematically study the cold interstellar medium of galaxies in the local universe. The survey observed an 850 μm dust continuum with SCUBA-2 for a sample of 193 *Herschel*-selected galaxies with $\log(M_*/M_\odot) > 9$ and integrated ^{12}CO(2–1) line fluxes with RxA3m for a subset of 97 of these galaxies. Of the 97 galaxies, 63 are within the footprint of MaNGA.

We briefly summarize the sample selection of JINGLE here. The JINGLE parent sample consists of $\sim$2800 galaxies with $\log(M_*/M_\odot) > 9$ and $0.01 < z < 0.05$ within the North Galactic Pole (NGP) region and three of the equatorial Galaxy And Mass Assembly (GAMA) fields (GAMA09, GAMA12, and GAMA15). The sample is narrowed down to $\sim$280 galaxies with a $>3\sigma$ detection at both 250 and 350 μm in the *Herschel* ATLAS survey that are predicted to be detectable with SCUBA-2 in less than 2 hr of integration. Then, 193 galaxies are selected in order to have a uniform stellar mass distribution at $\log(M_*/M_\odot) > 9$. A subsample of 97 galaxies predicted to be detectable in an on-source time of 345 minutes are selected to obtain integrated ^{12}CO(2–1) line fluxes. Two methods are used to estimate the flux and integration time for ^{12}CO(2–1) observations. The first method is the same as that used for the PI programs in Section [2.1.1](#). The second approach is based on the 2-Star Formation Mode formal flux prediction of Sargent et al. ([2014](#)), in which the ^{12}CO(1–0) line flux is related to the galaxy's position in the SFR–M_* plane. The predicted fluxes from the two methods agree well with each other. We note that JINGLE adopts an R_{21} of 0.7 for the required sensitivity and observing time estimation. More details on the JINGLE design, as well as the sample selection and

science goals, are given by Saintonge et al. ([2018](#); overview of the survey), M. W. L. Smith et al. (2018, in preparation; details of dust observations), and T. Xiao et al. (2018, in preparation; details of molecular gas observations).

We apply the same criteria to select galaxies in pairs as described in Section [2.1.1](#) ($r_p < 50$ kpc h^{-1} and $\Delta V < 500$ km s^{-1}, or P-merger > 0.4 and P-CS > 0.6) to the 45 JINGLE galaxies for which CO data were obtained before 2017 August.[27] A total of five galaxies in pairs are identified in this way, all of them through the r_p and ΔV criteria. The data reduction is carried out in the same way as our PI programs, described in Section [2.1.1](#).

2.1.3. Pair Sample: JINGLE Pilot

The JINGLE Pilot program (Y. Gao et al. 2018, in preparation) is a series of ^{12}CO (2–1) and (1–0) observations of MaNGA galaxies carried out by multiple facilities including JCMT, the 14 m telescope of the Purple Mountain Observation (PMO), and the 10.4 m telescope of the Caltech Submillimeter Observatory (CSO). The project was designed as a test of the JINGLE survey.

Galaxies were selected from the MaNGA MPL-3 (720 galaxies). The CO flux estimation for the MPL-3 galaxies also made use of the $L_{12\,\mu m}$–M_{H_2} relation as described in Section [2.1.1](#). A sample of 31 galaxies was selected for observations. The redshift range of these galaxies is 0.02–0.04. The galaxies were assigned to the various telescopes listed above according to the required sensitivity and the sensitivities of the telescopes. Some galaxies were observed by multiple telescopes to obtain both ^{12}CO(1–0) and ^{12}CO (2–1) data. The multiple transitions can be used to trace the physical conditions (e.g., temperature and density) of molecular gas.

There were 21 galaxies assigned to be observed by JCMT at ^{12}CO(2–1). The observations were done with the RxA receiver[28] between 2015 March and 2015 November, with a typical sky opacity of $\sim$0.12–0.32. A total of 17 galaxies were assigned to the PMO 14 m telescope at ^{12}CO(1–0). Observations were carried out in the winter of 2015 with the nine-beam receiver. The beam size of PMO observations at 115 GHz is 52″, which can cover the entire galaxy at the typical redshift of the sample. Three galaxies were observed by the CSO at ^{12}CO(2–1) with the Heterodyne receiver in 2015 February. The beam size of the CSO at 230 GHz is 30″. The full design of the project and details of the data reduction are presented in Y. Gao et al. (2018, in preparation).

From a total of 31 galaxies in the JINGLE Pilot sample, we identify five additional galaxies in pairs for our analysis based on the criteria described in Section [2.1.1](#), with two from JCMT, two from PMO, and one from CSO observations. Of these, four are selected based on r_p and ΔV and one based on Galaxy Zoo classification.

2.1.4. Pair Sample: xCOLD GASS

We also include galaxies in pairs from the Extended CO Legacy Database for GASS (xCOLD GASS; Saintonge et al. [2017](#)), an

---

[27] For reference, the number of galaxies in the first CO data release will be 72 (T. Xiao et al. 2018, in preparation).

[28] Observations taken at 230 GHz at the JCMT prior to 2015 December were taken with RxA. Observations taken after this date (specifically, after 2016 May 13) are observed with a replacement mixer. The JCMT thus calls the new instrument RxA3m.

extension of the IRAM 30 m legacy survey COLD GASS (Saintonge et al. 2011) that studies the molecular gas of nearby late-type galaxies with stellar masses $10 < \log(M_*/M_\odot) < 11.5$ and redshift $0.0025 < z < 0.05$. The xCOLD GASS survey extends the sample to $\log(M_*/M_\odot) = 9.0$. COLD GASS and xCOLD GASS observe galaxies in $^{12}CO(1-0)$ and $^{12}CO(2-1)$ with IRAM and complementary observations from APEX $^{12}CO(2-1)$. The $^{12}CO(1-0)$ data are used for this work because the beam size is exactly the same as for the JCMT 15 m telescope at 230 GHz.

We identify 27 galaxies in pairs from all 532 xCOLD GASS galaxies. The criteria for selecting galaxies in pairs are the same as described in Section 2.1.1 ($r_p < 50 \, \text{kpc} \, h^{-1}$ and $\Delta V < 500 \, \text{km} \, \text{s}^{-1}$, or P-merger >0.4 and P-CS >0.6). A total of 27 galaxies in pairs are identified, and all of them are identified through the r_p and ΔV criteria.

We have checked whether the galaxies from various observations reach different depths in terms of sensitivity. The main difference between the sample selection for the PI program/JINGLE/JINGLE Pilot and xCOLD GASS is the sensitivity (integration time) estimation. The former use the value of SFR/M_{H_2}, while the latter uses M_{H_2}/M_*. The M_{H_2}/M_* limit is 2.5% for xCOLD GASS (Saintonge et al. 2017). For the galaxies from the PI programs, JINGLE, and JINGLE Pilot, the typical M_{H_2}/M_* achieved is 3.3%, assuming $R_{21} = 0.6$, $\alpha_{CO} = 4.3$ (as the values used in Section 2.1.1), and a common line width of 300 km s^{-1}. We thus conclude that the samples analyzed here have comparable depth.

2.1.5. Pair Sample: Summary

In summary, our sample consists of a total of 58 galaxies in pairs (Table 2), of which 21 are from the JCMT PI programs, five from JINGLE, five from the JINGLE Pilot program, and 27 from xCOLD GASS. Fifty-six galaxies are selected based on r_p and ΔV and two (one from the PI program and one from the JINGLE Pilot program) based on Galaxy Zoo morphologies. It is important to note that the Galaxy Zoo classification could potentially pick up galaxies in the post-coalescence stage (i.e., post-merger). This is not the case for the two galaxies identified through their morphologies; in other words, our sample does not contain post-mergers. We refer the reader to Ellison et al. (2013, 2018), Thorp et al. (2019), and M. Sargent et al. (2018, in preparation) for the star formation and cold gas properties of post-mergers.

For the two galaxies identified through Galaxy Zoo morphologies, we estimate their r_p by calculating the distance between the two galactic nuclei. The distributions of galaxy properties are shown in Figure 1. Their merger properties are presented in Figure 2 (open and hatched histograms).

2.2. Control Sample: xCOLD GASS

In order to quantify the effect of galaxy interactions on star formation and molecular gas properties, isolated galaxies are used as a comparison sample to our galaxies in pairs. Isolated galaxies are selected from xCOLD GASS and are systems that have no spectroscopic companion within $r_p < 50 \, \text{kpc} \, h^{-1}$ and $\Delta V < 500 \, \text{km} \, \text{s}^{-1}$ and a P-merger value equal to zero. We use the same criteria to control the morphology of the control sample as described in Section 2.1.1. Combining these criteria yields a control sample pool of 154 galaxies. About 8% of the selected control galaxies have no detection in $^{12}CO(1-0)$. An
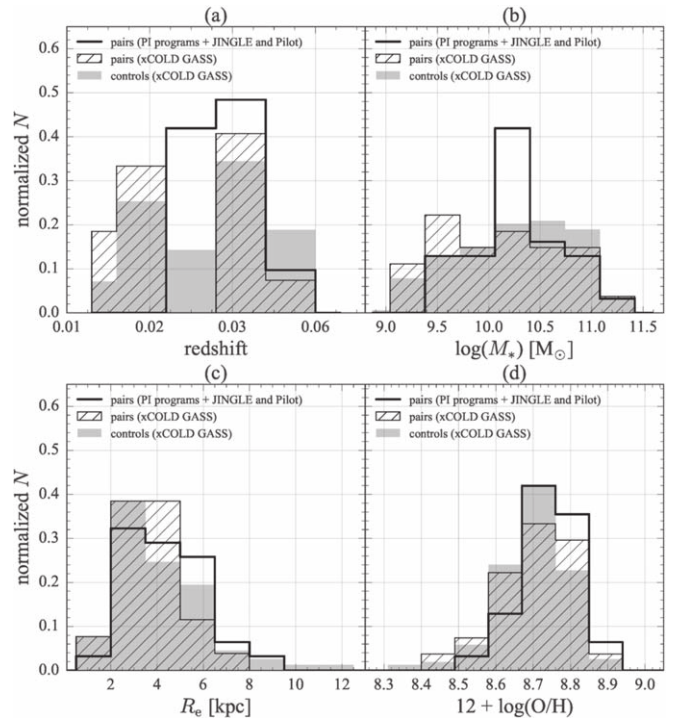
Figure 1. Histograms showing the distribution of the sample galaxies in terms of (a) redshift, (b) stellar mass, (c) effective radius measured at the r band, and (d) gas-phase metallicity. The open histograms represent galaxies in pairs from the PI programs, JINGLE, and JINGLE Pilot. The hatched histograms show the galaxies in pairs from the xCOLD GASS survey. The pool of controls is shown as filled histograms.

upper limit for the flux of 3σ is given for these galaxies (Saintonge et al. 2017). Since the integration limit M_{H_2}/M_* is as deep as 2.5% for xCOLD GASS, these nondetected galaxies thus truly have a lower gas fraction compared to other galaxies. These galaxies with upper limits for L_{CO} are included in the analysis. All of our conclusions remain unchanged if we use only galaxies with detections. The distributions of the galaxy properties of controls are shown in Figure 1 (filled histograms).

2.3. Aperture Correction

Some of the galaxies have optical sizes in excess of the telescope beams, so an aperture correction is required to correct the measured CO fluxes and turn them into estimates for the total flux. For reference, the range in the effective radius (R_e; Petrosian half-light radius measured at the r band) of our sample is $\sim$2–6 kpc, as shown in Figure 1(c), corresponding to about $4''$–$12''$ at the redshifts of our sample (Figure 1(a)).

Aperture corrections are applied to all galaxies in pairs and control galaxies in this study. We adopt the method of Saintonge et al. (2012). For each galaxy, we create a model galaxy having an exponential molecular gas distribution with a profile following that of the stellar light. This assumption is based on the observation that CO and SFR distributions trace each other well in nearby galaxies (Leroy et al. 2009). Then, the model is convolved with a Gaussian matching the properties of the telescope beams. The aperture correction is the ratio between the total flux of the model and the flux in the beam area. The median aperture correction to the CO luminosity across the galaxies in pairs and the pool of controls are 0.09 and 0.08 dex, receptively.

Table 2
Physical Properties of Galaxies in Pairs

Source	z	$\log(M_*)$ $(M_\odot)$	$\log(SFR)$ $(M_\odot\ yr^{-1})$	R_e (kpc)	r_p (kpc)	μ	$L_{CO}/10^8$ (K km s^{-1} pc^2)	$12+\log(O/H)$	α_{CO} $(M_\odot/L_{CO})$	Parent Sample
(1)	(2)	(3)	(4)	(5)	(6)	(7)	(8)	(9)	(10)	(11)
J130125.07+284038.0	0.029	10.23	0.33	8.3	27.88	1.76	7.39(0.49)	8.82	2.22	J
J130615.12+252737.9	0.024	10.12	0.37	6.1	16.81	0.63	7.71(0.91)	8.76	2.85	J
J132035.40+340821.7	0.023	10.29	0.82	8.6	31.61	1.28	89.94(1.0)	8.71	3.62	J
J132443.68+323225.0	0.04	10.84	1.07	9.0	60.18	0.88	29.42(2.97)	8.75	3.07	J
J133457.27+340238.7	0.024	10.56	0.64	12.4	40.94	0.19	30.91(2.23)	8.86	1.91	J
J075641.84+175928.2	0.041	10.57	1.03	4.9	26.61	0.87	14.16(1.46)	8.76	3.0	xCG
J081115.92+251045.7	0.014	9.62	−0.38	7.8	29.08	0.74	0.52(0.08)	8.65	4.25	xCG
J081905.10+214729.0	0.015	10.08	0.11	62.0	62.12	0.62	54.17(0.44)	8.69	3.73	xCG
J084256.38+133829.7	0.017	9.68	0.31	12.4	4.95	0.04	2.3(0.21)	8.7	3.83	xCG
J085254.99+030908.4	0.035	10.28	−0.04	4.0	63.95	1.1	1.58(0.32)	8.61	5.02	xCG
J090311.25+100907.0	0.03	10.11	0.3	9.6	51.6	0.53	5.83(0.58)	8.84	2.11	xCG
J093236.58+095025.9	0.049	10.86	0.67	5.1	71.02	0.04	9.77(1.35)	8.52	7.29	xCG
J095324.56+074956.2	0.039	10.67	−0.36	4.2	61.17	0.82	2.44(0.54)	8.68	3.51	xCG
J103333.43+115216.9	0.034	10.59	0.76	5.4	12.99	0.63	16.39(1.46)	8.79	2.61	xCG
J104024.66+065137.7	0.03	10.89	0.07	6.8	68.8	0.31	8.91(0.78)	8.55	6.11	xCG
J112746.27+265734.5	0.033	10.6	−0.94	4.6	63.77	1.64	2.02(0.41)	8.62	4.22	xCG
J112946.35+152001.1	0.037	11.02	−0.76	6.3	70.29	1.64	4.88(0.74)	8.67	3.32	xCG
J113116.03+043908.7	0.033	10.09	0.47	7.1	47.21	1.07	6.51(0.65)	8.87	1.92	xCG
J113701.89+153414.1	0.013	9.88	−0.52	15.4	45.25	1.44	1.84(0.16)	8.76	2.71	xCG
J113914.72+145932.7	0.014	9.64	−0.36	5.1	47.96	1.21	0.58(0.08)	8.71	3.4	xCG
J115020.17+255742.7	0.013	9.36	−0.21	11.7	30.97	0.88	0.49(0.07)	8.44	10.33	xCG
J115726.68+251359.0	0.015	9.37	−0.73	7.1	48.58	−1.15	0.45(0.09)	8.76	2.75	xCG
J120222.51+295142.3	0.01	9.98	−0.16	8.8	55.07	0.76	5.91(0.5)	8.77	2.69	xCG
J120409.73+014933.5	0.017	9.67	−0.21	10.5	31.51	−0.9	1.18(0.18)	8.8	2.41	xCG
J125905.29+273839.9	0.018	9.67	0.09	6.6	40.87	−0.26	1.98(0.21)	8.82	2.32	xCG
J130750.80+031140.7	0.039	11.12	−0.42	7.9	43.51	2.03	7.41(0.78)	8.7	3.04	xCG
J134701.23+335336.9	0.017	9.78	−0.31	16.0	26.29	0.29	1.21(0.15)	8.64	4.46	xCG
J135655.41+140832.1	0.015	9.31	−0.81	9.5	59.52	0.9	0.64(0.11)	8.64	4.28	xCG
J142342.38+340032.4	0.013	9.84	−0.02	8.4	14.95	−0.18	2.46(0.2)	8.77	2.72	xCG
J143525.34+002003.5	0.035	10.2	0.71	3.7	66.43	0.89	12.2(1.11)	8.79	2.66	xCG
J225258.55+010833.3	0.016	9.5	−0.7	10.3	58.37	−0.87	0.58(0.08)	8.6	5.12	xCG
J231229.22+135632.1	0.034	10.91	−0.49	5.4	51.67	0.37	8.23(0.92)	8.67	3.51	xCG
J025057.46+002209.8	0.044	10.05	0.63	3.1	26.08	−0.13	3.34(0.79)	8.8	2.58	PI
J031943.04+003355.7	0.024	10.06	0.27	7.6	44.48	−0.75	1.83(0.66)	8.73	3.19	PI
J032043.18−010008.2	0.036	10.64	0.68	5.5	12.15	1.14	35.82(1.69)	8.75	2.97	PI
J032247.22+000857.7	0.023	10.38	−1.29	13.7	32.19	1.18	6.77(0.77)	8.67	3.38	PI
J075454.46+535046.5	0.035	10.76	0.7	6.0	60.07	1.69	21.41(1.21)	8.72	3.4	PI
J082150.16+453110.6	0.054	10.38	0.77	3.4	59.25	0.73	14.95(1.02)	8.85	2.07	PI
J093846.17+483346.3	0.025	9.43	0.11	5.4	20.88	−0.94	3.1(0.43)	8.71	3.6	PI
J100508.31+443050.5	0.026	10.36	−0.74	9.6	65.66	0.38	3.65(1.37)	8.66	3.75	PI
J100718.98+463247.1	0.024	10.17	0.03	7.1	37.5	1.44	5.14(0.72)	8.82	2.17	PI
J102843.06+395019.9	0.029	9.95	0.45	3.5	38.56	0.53	4.22(1.25)	8.82	2.37	PI
J102855.10+395341.3	0.044	10.26	−0.0	6.2	27.37	0.5	13.15(1.07)	8.71	3.32	PI
J121049.28+440345.3	0.023	10.18	−0.12	5.3	41.8	1.5	1.16(0.14)	8.73	3.09	PI
J130420.70+450323.9	0.028	9.66	0.34	7.2	62.3	0.63	5.07(0.67)	8.65	4.6	PI
J134109.43+231640.5	0.027	9.88	−0.16	3.1	13.98	−0.66	12.21(1.31)	8.75	2.94	PI
J135129.47+434823.1	0.033	10.16	0.61	4.4	43.84	1.33	6.77(1.0)	8.71	3.62	PI
J140057.82+425120.3	0.032	10.67	0.49	6.0	25.33	0.0	13.17(1.04)	8.76	2.84	PI
J153545.82+445005.2	0.03	10.19	0.47	8.8	49.31	1.03	8.9(1.35)	8.78	2.66	PI
J154219.34+475636.7	0.037	9.65	−0.36	3.7	15.87	−0.33	12.28(0.79)	8.67	3.94	PI
J160242.58+411150.1	0.033	10.41	0.69	7.8	17.46	0.42	22.59(2.2)	8.82	2.31	PI
J163349.62+391547.5	0.032	10.74	0.42	6.2	32.83	1.01	10.68(0.8)	8.73	3.1	PI
J172823.84+573243.4	0.029	9.61	0.8	3.9	7.79	...	5.48(0.81)	8.51	8.47	PI
J032042.95−010631.1	0.021	10.02	−0.04	11.6	55.22	0.9	3.92(0.26)	8.79	2.47	JP
J074637.71+444725.8	0.031	11.16	0.2	9.3	33.58	0.6	39.69(2.53)	8.67	3.8	JP
J091500.75+420127.8	0.028	10.27	0.87	4.9	61.02	−0.35	9.48(1.85)	8.76	3.01	JP
J091555.53+441957.9	0.04	10.95	1.23	10.4	9.73	...	46.21(4.58)	8.78	2.81	JP
J110637.36+460219.5	0.025	10.44	0.52	4.3	27.03	1.76	14.81(1.65)	8.77	2.76	JP

Note. Column (1) SDSS ID; column (2) SDSS spectroscopic redshift; column (3) stellar mass from the MPA-JHU Catalog (Section 2.4); column (4) SFR from the MPA-JHU Catalog (Section 2.4); column (5) NSA 50% light radius measured at the r band; column (6) projected separation between two galaxies in a pair; column (7) stellar mass ratio between two galaxies in a pair (Section 2.5); column (8) aperture- and line ratio–corrected ($R_{21} = 0.8$) CO luminosity L_{CO} and its uncertainty (Section 2.3); column (9) gas-phase metallicity (Section 2.6); column (10) CO-to-H$_2$ conversion factor (Section 3.1); column (11) parent samples (Section 2.1), where J = JINGLE (Section 2.1.2), xCG = xCOLD GASS (Section 2.1.4), PI = PI programs (Section 2.1.1), and JP = JINGLE Pilot (Section 2.1.3).
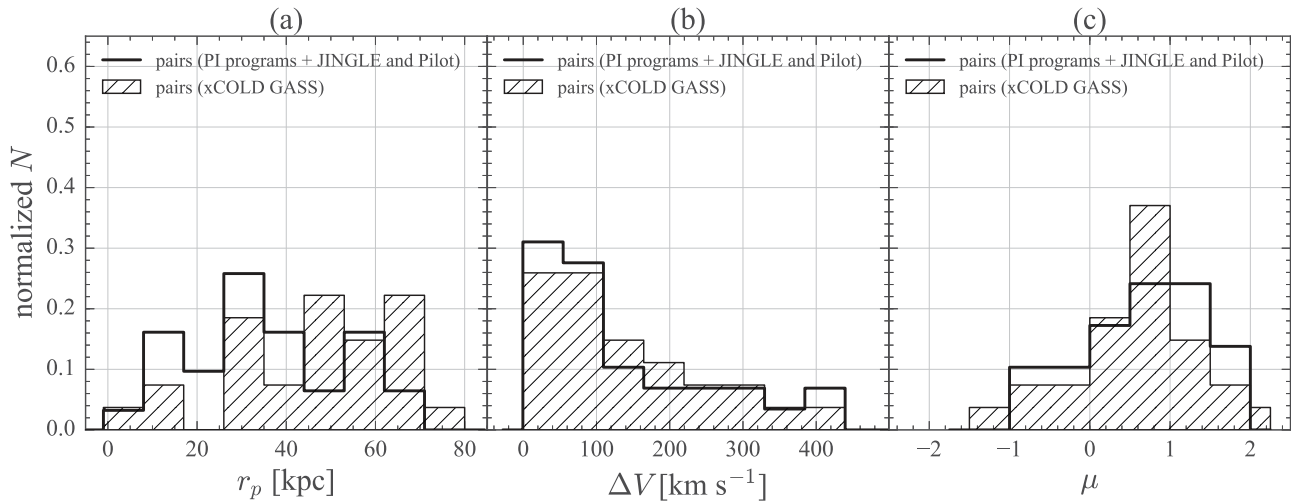
Figure 2. Distributions of merger configurations across the galaxies in pairs from the PI programs, JINGLE, and JINGLE Pilot (open histograms) and xCOLD GASS (hatched histograms): (a) projected separation of the two galaxies, (b) line-of-sight velocity difference, and (c) stellar mass ratio.

2.4. Global Stellar Mass and SFR

The global SFR and M_* are taken from the MPA-JHU DR7 public catalog.[29] The MPA-JHU catalog assumes a Kroupa IMF (Kroupa 2001). Here M_* is estimated by fitting stellar population models from Bruzual & Charlot (2003) to the *ugriz* SDSS photometry, following the method of Kauffmann et al. (2003a). The M_* values have been found to agree with other estimates (e.g., Taylor et al. 2011; Mendel et al. 2014; Chang et al. 2015). To estimate SFRs, Brinchmann et al. (2004) first distinguished the emission-line properties based on the theoretical upper (lower) limit for pure starburst (AGN) models (Kewley et al. 2001; Kauffmann et al. 2003b) on the Baldwin–Phillips–Terlevich (BPT) diagram (Baldwin et al. 1981). For galaxies in which the primary source of ionizing photons is from H II regions, SFRs are estimated by fitting a grid of photoionization models from Charlot & Longhetti (2001) to the observed Hα, Hβ, [O III], and [N II] line fluxes. These SFR estimates agree well with those derived from the infrared fluxes (Charlot et al. 2002). For galaxies falling outside of the star-forming regime on the BPT diagrams, since the line fluxes might be affected by the AGN component, their SFRs are estimated based on the relation between specific SFR (sSFR = SFR/M_*) and D4000 (Brinchmann et al. 2004). This relationship was constructed using the sSFR and D4000 of star-forming galaxies. According to the BPT diagram, the pair sample consists of eight AGNs, 11 composites, and 39 star-forming galaxies. The pool of the control sample includes 31 AGNs, 34 composites, and 89 star-forming galaxies. It is worth noting that by adopting currently popular modified-BPT diagrams to distinguish Seyfert and low-ionization emission-line (nuclear) regions (LI(N)ERs) in the AGN regime (Cid Fernandes et al. 2013), the majority of the AGNs in our sample (six out of eight for galaxies in pairs and 27 of the controls) are LI(N)ERs, which could in fact be powered by stellar populations instead of a nuclear compact source (Belfiore et al. 2016; Hsieh et al. 2017).

The aperture corrections are determined for these central SFR measurements by fitting the photometry of the outer regions of the galaxies (Salim et al. 2007). In the following analysis, the median SFR and M_* from the probability distributions for each galaxy are used. Using the average SFR and M_* does not change the results.

The distribution of the pair sample in the SFR versus M_* plane is shown in Figure 3 with colored symbols. Galaxies taken from the control sample drawn from xCOLD GASS are represented by gray squares. Gray dots are the remaining xCOLD GASS targets not selected as control, for reference.

2.5. Mass Ratio of Pairs

Pairs in this work contain both primary (higher-M_* galaxy in a pair) and secondary (lower-M_* galaxy) galaxies. For each pair, we define the mass ratio as the stellar mass of the CO-observed galaxy divided by that of its companion and take the logarithm of the ratio (μ). A positive value of μ implies that the observed galaxy is the primary galaxy in the pair, and vice versa. A few companions do not have the MPA-JHU measurement for M_*. In this case, the mass ratios of these systems are calculated using M_* from the NASA-Sloan Atlas catalog[30] for both galaxies. It is not possible to derive the mass ratio for the two pairs identified through Galaxy Zoo morphologies, as the two galaxies in the pairs are too close to have separated measurements. These two galaxies appear to be major mergers, and the CO observations are made toward the primary galaxies. They are excluded from the discussion involving mass ratio. The distribution of the mass ratio is shown in Figure 2(c).

2.6. Gas-phase Metallicity 12+log(O/H)

In this work, we adopt a metallicity-dependent α_{CO} (see Section 3.1). Gas-phase metallicity is calculated using the O3N2 method empirically calibrated by Pettini & Pagel (2004):

$$12 + \log(\text{O/H}) = 8.73 - 0.32\left(\frac{[\text{O III}]}{\text{H}\beta} \Big/ \frac{[\text{N II}]}{\text{H}\alpha}\right). \quad (2)$$
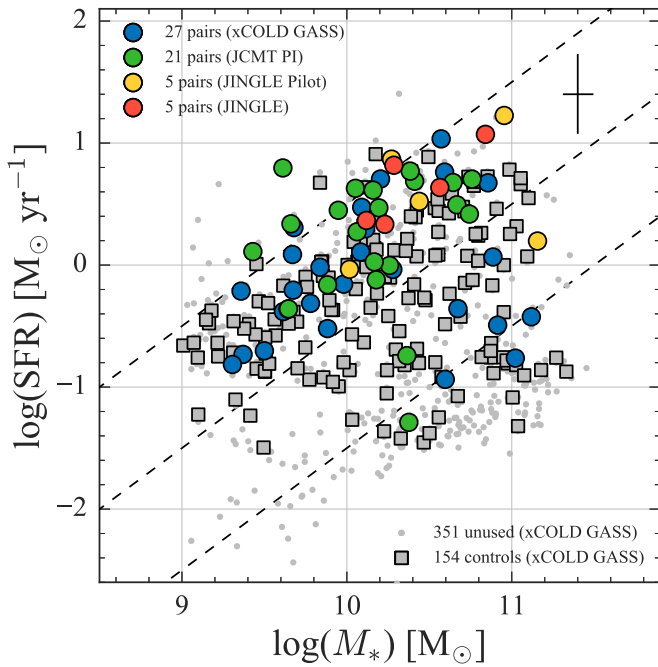
The emission-line fluxes are obtained from the MPA-JHU DR7 release.[31] All of the emission-line fluxes of our galaxies in pairs and controls have S/Ns higher than 3.5 if the flux uncertainties in

Figure 3. Global SFR vs. stellar mass relation of galaxies discussed in this work. Galaxies in pairs used in this work are shown as colored symbols. Galaxies from the control sample are shown as gray squares. Those in the xCOLD GASS sample that are not used in the analysis are shown as gray dots (see text for details). The SFR and M_* values are taken from the MPA-JHU catalog. From top to bottom, the three dashed lines correspond to $\log(\mathrm{sSFR/yr^{-1}}) = -9.5, -10.5,$ and -11.5.

the catalog are used or higher than 2 (mostly ≫5) if the scaling factors[32] provided in the MPA-JHU DR7 website are applied to the flux uncertainties, which were calculated by the comparisons of the derived line fluxes of galaxies that were observed multiple times. Since these emission lines are close in wavelength, dust extinction should have a minimal effect on the fluxes. Galaxies in pairs and controls have similar ranges of metallicity, from 8.3 to 8.9. The median values are 8.7 for both populations (Figure 1(d)).

3. Results

3.1. SFR and Gas Properties in the Full Pair Sample

To get an idea of the distribution of galaxy properties within our sample, we first show the normalized distribution of galaxy sSFR, L_{CO}, and gas properties. In cases where the CO line is undetected, the 3σ upper limits of L_{CO} luminosity (Section 2.2) are used for the analysis and plots in this paper.

Figure 4(a) shows the distribution of sSFR in the pair sample as a filled histogram and for the control sample as an open histogram. While the two distributions peak at the same sSFR, the median sSFR of galaxies in pairs ($\log(\mathrm{sSFR/yr^{-1}}) = -9.9$) is higher than that of isolated galaxies ($\log(\mathrm{sSFR/yr^{-1}}) = -10.3$). We check whether the distributions in Figure 4(a) are sampled from the same parent distribution. This is tested with the Kolmogorov–Smirnov (K-S) statistic, whose results are listed in Table 3. The K-S test returns a p-value $= 1.9348 \times 10^{-5}$, suggesting a >99.9% probability that the sSFRs of

[32] The scaling factors are 2.473, 1.882, 1.566, and 2.039 for the Hα, Hβ, [O III], and [N II] lines, respectively.

galaxies in pairs and controls are two distinct distributions. This is in agreement with the many previous studies that have found enhanced star formation in galaxies in pairs (e.g., Di Matteo et al. 2007; Ellison et al. 2008; Scudder et al. 2012; Patton et al. 2013; Knapen et al. 2015). In Sections 3.3 and 3.4, we return to SFR differences as a function of projected separation and mass ratio, respectively.

Turning now to gas properties, in Figure 5(a), we first show the comparison of the integrated L_{CO} of galaxies in pairs and controls. From this figure, it is evident that galaxies in pairs (filled histogram) show higher L_{CO} compared to the pool of controls (open histogram). The difference is significant. The K-S test results in a p-value of 0.0017.

After having looked at the observed quantity L_{CO}, we now derive the physical quantities of gas from the measurements. The distribution of $M_{\mathrm{H_2}}$ is shown in Figure 4(b). Here L_{CO} is converted to $M_{\mathrm{H_2}}$ by multiplying by the conversion factor, α_{CO}. The value for α_{CO} is calculated following Accurso et al. (2017), in which α_{CO} is metallicity-dependent, with a second-order dependence on the offset of a galaxy from the star-forming main sequence,

$$\log \alpha_{\mathrm{CO}}(\pm 0.165) = 15.623 - 1.732[12 + (\mathrm{O/H})]$$
$$+ 0.051 \log \Delta(\mathrm{MS}), \qquad (3)$$

where $\Delta(\mathrm{MS})$ is the distance off the analytical definition of the main sequence by Whitaker et al. (2012). No significant difference in the ranges and median values of α_{CO} is found between galaxies in pairs and controls. The derived α_{CO} values are in the range of 1.9–10.3 $M_\odot$ (K km s^{-1} pc^2) for the galaxies in pairs (Table 2) and 2.1–16.5 $M_\odot$ (K km s^{-1} pc^2) for the controls. The median α_{CO} values are 3.0 and 3.2 $M_\odot$ (K km s^{-1} pc^2) for galaxies in pairs and controls, respectively. The distributions of $M_{\mathrm{H_2}}$ for the galaxies in pairs and controls largely overlap, but the peak $M_{\mathrm{H_2}}$ of galaxies in pairs is higher than that of controls. The median $\log(M_{\mathrm{H_2}}/M_\odot)$ values of galaxies in pairs and controls are 9.3 and 8.9, respectively. According to the K-S test, the differences between galaxies in pairs and controls are real: the probability that their $M_{\mathrm{H_2}}$ values are from the same distribution is less than 1% (p-value = 0.0016).

The f_{gas} and SFE are calculated based on the derived $M_{\mathrm{H_2}}$. The gas fraction f_{gas} is defined as

$$f_{\mathrm{gas}} = \frac{M_{\mathrm{H_2}}}{M_{\mathrm{H_2}} + M_*}. \qquad (4)$$

Note that some studies adopt the definition of $f_{\mathrm{gas}} = M_{\mathrm{H_2}}/M_*$. The two definitions are approximately the same when $M_{\mathrm{H_2}} \ll M_*$ (i.e., low f_{gas}). Our results would be qualitatively the same if we adopted this definition. Figure 4(c) shows the normalized distribution of the molecular gas fraction. The $\log(f_{\mathrm{gas}})$ of the controls (open histogram) spans the range -2.37 to 0.64 (corresponding to 0.4%–22.9%) with a median value of -1.26 (5.5%). The values are consistent with other studies of galaxies in the local universe (e.g., Leroy et al. 2008; Bothwell et al. 2009; Saintonge et al. 2017). On the other hand, the range of $\log(f_{\mathrm{gas}})$ of galaxies in pairs (filled histogram) shifts to larger values, from -1.81 to -0.20 (1.5%–63.1%), with a median value of -1.03 (9.3%). A K-S test of f_{gas} yields a
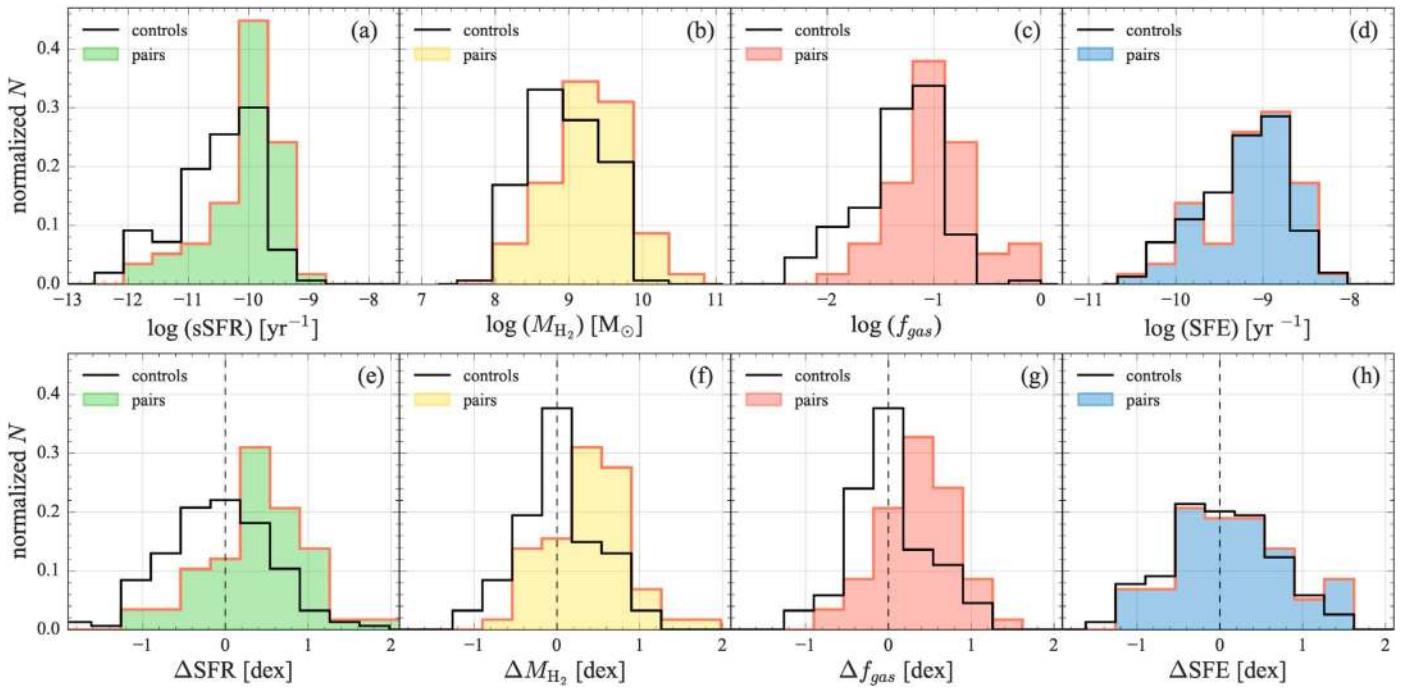
Figure 4. Histograms showing the distribution of the physical quantities sSFR, M_{H_2}, f_{gas}, and SFE in the upper row and the offset of these properties with respect to the control sample in the lower row. The galaxies in pairs and controls are plotted as filled and open histograms, respectively. The vertical dashed lines in the lower panels indicate zero enhancement. The enhancements of SFR, M_{H_2}, and f_{gas} are observed to be statistically significant for both raw and offset quantities (Table 3). The strength of the SFE offset is not as large as that of other properties, and a K-S test suggests that the difference is not significant.

Table 3
Summary of the K-S Test Results for Galaxies in Pairs and Controls

	Raw Value (Section 3.1)	Offset Value (Δ) (Section 3.2)
(s)SFR	1.9348×10^{-5}	8.2130×10^{-6}
L_{CO}	0.0017	4.3003×10^{-5}
M_{H_2}	0.0016	1.1890×10^{-6}
f_{gas}	3.9535×10^{-7}	8.7772×10^{-7}
SFE	0.2128	0.4806

p-value $= 3.9535 \times 10^{-7}$. There is less than a 0.1% chance that the two samples come from the same distribution.

The SFE is defined as

$$\frac{\text{SFE}}{(\text{yr}^{-1})} = \frac{\text{SFR}}{M_{H_2}} \qquad (5)$$

and is shown in Figure 4(d). The ranges and peaks of SFE appear closely matched for galaxies in pairs and controls. Median $\log(\text{SFE}/\text{yr}^{-1})$ values are -9.02 and -9.13 for galaxies in pairs and controls, respectively. The values of SFE are comparable with those of other studies of nearby isolated galaxies (e.g., Leroy et al. 2008; Koyama et al. 2017). A K-S test suggests that the two samples are drawn from the same distribution (p-value $= 0.2128$).

We have shown in this section that there are statistically significant differences in SFR, M_{H_2}, and f_{gas} between the galaxies in pairs and the full control sample, and that there is no significant difference in SFE between these two populations. However, we have not yet considered possible differences in the fundamental properties of these two samples, such as stellar mass and redshift. Since the SFR and gas properties themselves depend on these underlying characteristics, a rigorous
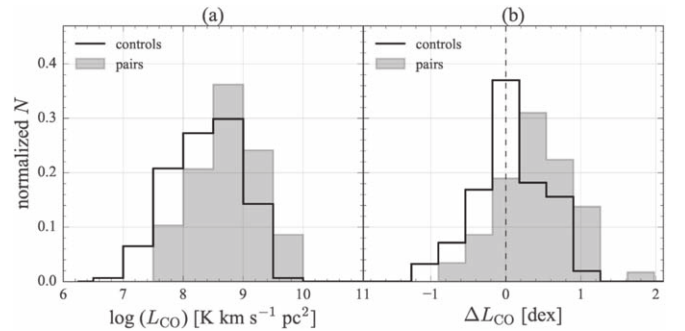
Figure 5. Distributions of (a) L_{CO} and (b) ΔL_{CO}. The galaxies in pairs and controls are plotted as filled and open histograms, respectively. The vertical dashed line in panel (b) indicates zero enhancement. The figures confirm that the enhancement of the M_{H_2} and f_{gas} of gas in galaxies in pairs is already indicated from the comparison from the observed quantity L_{CO}, i.e., before the conversion to M_{H_2}.

comparison requires a careful matching between the galaxies in pairs and the control sample. We investigate this in the following section.

3.2. Offset of SFR and Gas Properties

In order to fairly compare the properties of the galaxies in pairs and controls on a galaxy-by-galaxy basis, and accounting for dependences on properties such as redshift and M_*, we compute "offset" quantities in this section. Our approach closely follows that of Violino et al. (2018) for H_2 fractions in a smaller sample of galaxies in pairs, as well as that of Ellison et al. (2018) for H I fractions in post-mergers. Each galaxy, including pairs and controls, is matched in redshift, stellar mass, and effective radius with a minimum of five control galaxies from the pool of controls. The tolerance of stellar
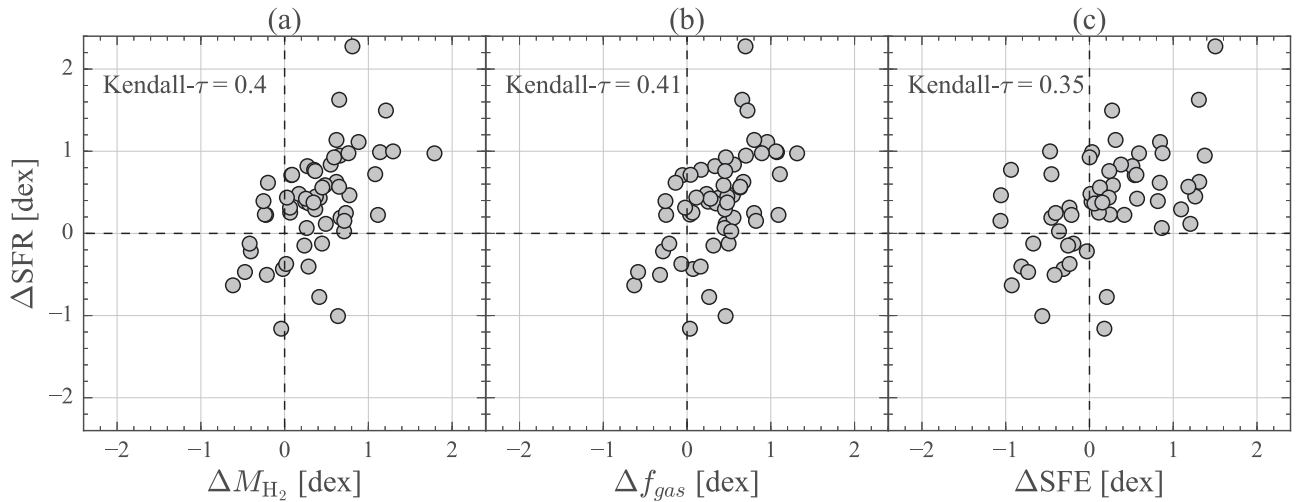
Figure 6. (a) ΔSFR vs. ΔM_{H_2}, (b) Δf_{gas}, and (c) ΔSFE of the galaxies in pairs. The dashed lines indicate zero enhancement. The Kendall's τ correlation coefficient between two variables is given in the upper left corner of each panel. The figure indicates that all molecular gas properties (M_{H_2}, f_{gas}, and SFE) are expected to influence SFR.

mass, redshift, and effective radius are 0.1 dex, 0.005, and 25%, respectively. The criteria are allowed to grow by 0.1 dex, 0.005, and 5%, respectively, until the minimum required number of control galaxies is reached. Most of the galaxies could find sufficient control galaxies in the first round. The "offset" of a galaxy property (P) is defined as

$$\Delta(P) = \log(P_{gal}) - \log(\text{median}(P_{control})), \qquad (6)$$

where P_{gal} is the property of the galaxy in question and median($P_{control}$) is the median property of its control galaxies. We should emphasize that, as this is taken in the logarithm form, it really is a ratio of the value of the galaxy in question against the median value of its controls. A positive offset represents an enhancement, while a negative value implies a suppression of the property. Distributions of offset properties are presented in Figure 5(b) for L_{CO} and Figures 4(e)–(h) for other physical quantities related to SFR[33] and gas properties. Open and filled histograms denote the offset properties of controls and galaxies in pairs, respectively. The median values for the controls are around zero, as expected, the width showing the intrinsic spread of the quantities plotted.

The enhancement of SFR is still present and significant (p-value = 8.2130×10^{-6}; see Table 3), as indicated by the peaks of the distributions (Figure 4(e)). The median ΔSFR is 0.40 dex (a factor of $\sim$2.5 enhancement), confirming the well-known fact that, statistically, galaxy–galaxy interaction enhances the SFR, but not dramatically so; moreover, there is a large spread in the enhancement of SFR (e.g., Scudder et al. 2012; Knapen et al. 2015).

Figure 5(b) confirms that the enhancement of the amount of gas in galaxies in pairs is already indicated from the comparison from the observed L_{CO}, i.e., before the conversion to M_{H_2}. The K-S test yields a p-value of 4.3003×10^{-5}. The median ΔL_{CO} of galaxies in pairs is 0.40 dex.

The median ΔM_{H_2} and Δf_{gas} are enhanced by similar factors, about 0.37 and 0.44 dex, respectively (Figures 4(f) and (g)). We also apply the K-S test to the offset distributions of galaxies in pairs and controls. For M_{H_2} and f_{gas}, the K-S test gives a $<$1% probability of the two distributions being drawn from the same parent distribution (Table 3).
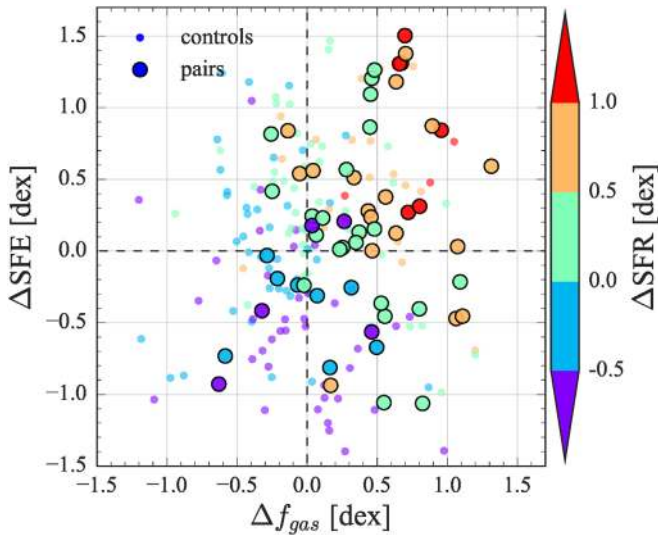
The strength of the SFE offset is not as large as that of other properties. The median ΔSFE implies an offset by 0.14 dex with respect to the controls. However, a K-S test suggests that the difference is not significant; there is a high probability that the two distributions (control and pairs) are drawn from the same population.

In order to investigate which gas property is most strongly correlated with SFR enhancement, in Figure 6 we plot Δf_{gas}, ΔM_{H_2} and ΔSFE versus ΔSFR. All gas property offsets increase with ΔSFR. We use Kendall's τ correlation coefficient to quantify the strength of the dependence. The computation yields positive correlations of 0.40, 0.39 and 0.35 for ΔM_{H_2}, Δf_{gas} and ΔSFE, respectively. Based on this figure, we can speculate that all molecular gas properties (M_{H_2}, f_{gas}, and SFE) are expected to influence SFR.

Figure 7 presents the ΔSFE versus Δf_{gas}, color-coded by ΔSFR. The large and small circles represent galaxies in pairs and controls, respectively. Various inferences can be drawn from this figure. The highest ΔSFRs predominantly occur in galaxies with both enhanced Δf_{gas} and enhanced ΔSFE; however, enhanced Δf_{gas} and ΔSFE together do not always result in a high magnitude of ΔSFR (but almost all galaxies with positive values of Δf_{gas} and ΔSFE show enhanced SFR). Galaxies may not have enhanced SFR if only f_{gas} or SFE is enhanced. Finally, galaxies associated with both suppressed SFE and f_{gas} are likely to have suppressed SFR as well.

3.3. ΔSFR, Δf_{gas}, and ΔSFE as a Function of Projected Separation

Figure 8(a) presents the ΔSFR of our galaxies in pairs as a function of r_p. Gray circles denote individual galaxies in pairs, and colored squares show the mean ΔSFR at different r_p bins. Error bars are obtained by calculating the sample standard deviation and dividing by $\sqrt{N}$, where N is the number of

---

[33] In Section 3.1, we use "sSFR" to express the absolute value of SFR so that the dependence of SFR on M_* is considered. The offset property of star formation is defined as the difference of "SFR" between galaxies in pairs and controls. The two SFRs are not different, as the M_* is matched when selecting the control sample to calculate the SFR offset.

Figure 7. The ΔSFE vs. Δf_{gas}, color-coded by ΔSFR. The large and small circles represent galaxies in pairs and controls, respectively. The highest ΔSFRs (>0.5 dex) predominantly occur in galaxies with both enhanced Δf_{gas} and enhanced ΔSFE; however, enhanced Δf_{gas} and ΔSFE together do not always result in a high magnitude of ΔSFR (but it is true that almost all galaxies with positive values of Δf_{gas} and ΔSFE show enhanced SFR). Galaxies may not have enhanced SFR if only f_{gas} or SFE is enhanced (upper left and lower right corners of the figure). Finally, galaxies associated with both suppressed SFE and f_{gas} are likely to have suppressed SFR as well (lower left corner of the figure).

galaxies at each r_p bin. The dashed horizontal line denotes zero enhancement. At small separations, galaxies in pairs are found to have substantially higher SFR than their controls, with median ΔSFR increasing from ≈ 0.2 dex at ~ 70 kpc to ~ 0.9 dex at <10 kpc. The fastest rise of ΔSFR occurs at $r_p \approx$ 20–30 kpc, as also shown in Scudder et al. (2012) and Patton et al. (2013) with much larger sample sizes than this work and in Bustamante et al. (2018) with cosmological simulations. The ΔSFR (0.9 ± 0.5 dex) in the lowest r_p bin is higher than that of post-mergers (0.5 ± 0.1 dex) in Ellison et al. (2013). This may be due to a mix of post-mergers that are already quenched and actively forming stars, as the SFR and duration of enhanced SFR at the coalescence phase depend on various merger configurations (e.g., Di Matteo et al. 2007, 2008; Bustamante et al. 2018; Thorp et al. 2019).

The enhanced SFR as two galaxies approach each other could be interpreted as direct evidence of tidally triggered star formation. Park & Choi (2009) investigated the dependence of galaxy properties on both the small- and large-scale environments. They found that galaxy properties, such as Hα equivalent width, surface brightness profile, and colors, abruptly change when r_p corresponds to the $0.05\times$ virial radius of the nearest-neighbor galaxy (see their Figures 6 and 7). This corresponds to ~ 20 kpc for the galaxies in their sample. This interpretation can be applied to our result of the boost of ΔSFR at $r_p \approx 20$–30 kpc. However, we should note that this characteristic radius depends on the stellar mass of the sample galaxies because the hydrodynamic interactions between galaxies depend on the stellar mass (Park & Choi 2009).

It should be noted that there is significant scatter within each r_p bin (see also Scudder et al. 2012). There are several reasons for the scatter. First, the peak in SFR enhancement does not always occur near coalescence. The SFR could reach the peak
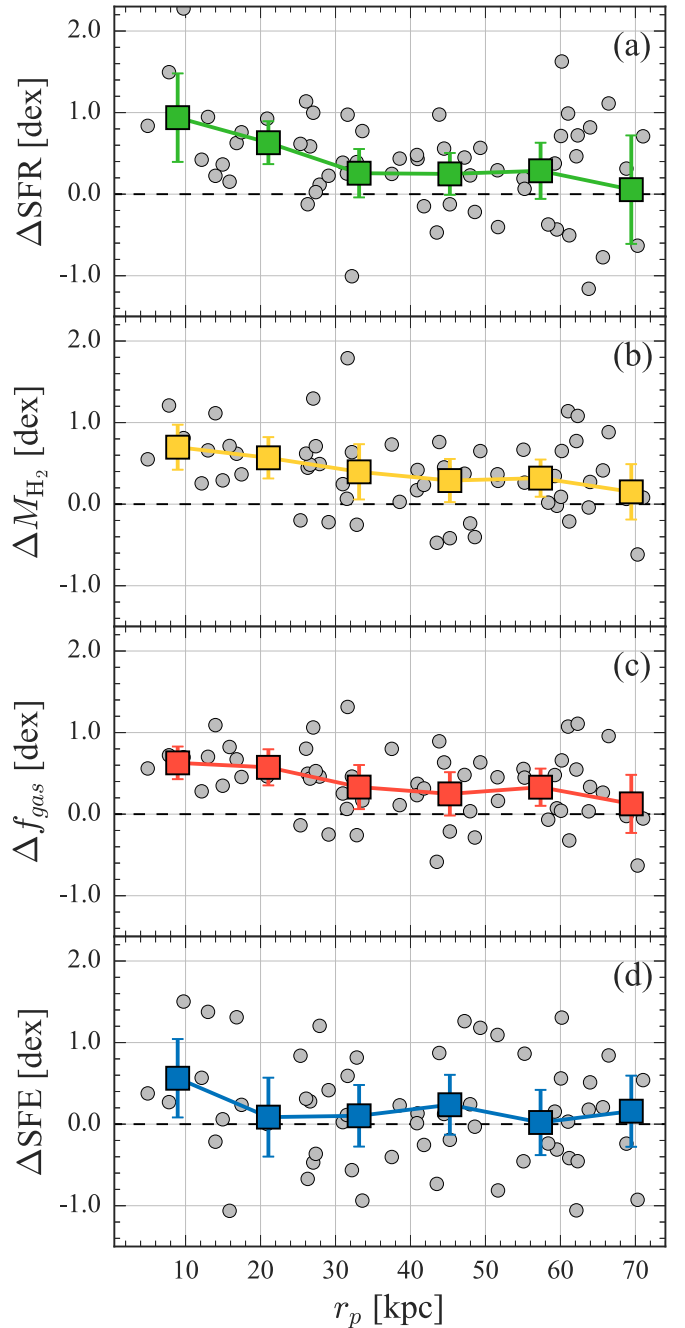
Figure 8. Offset properties as a function of projected galaxy separation for our sample. Gray circles denote individual galaxies. Mean values per r_p are indicated with colored squares. Error bars are obtained by calculating the sample standard deviation and dividing by $\sqrt{N}$, where N is the number of galaxies at each r_p bin. The horizontal lines indicate no enhancement. The ΔSFR, $\Delta M_{\mathrm{H_2}}$, and Δf_{gas} all increase with decreasing pair separation over the range from ~ 70 to 10 kpc. However, any SFE enhancement is only significant at the smallest pair separations.

when two galaxies are still several tens of kpc apart (Di Matteo et al. 2008; Sparre & Springel 2016). Moreover, ΔSFR depends on the mass ratio. This will be discussed in Section 3.4. Many studies have stressed the importance of the properties of the companion in determining the SFR enhancement (Park & Choi 2009; Hwang et al. 2010; Xu et al. 2012; Cao et al. 2016). Specifically, the SFRs of spirals in spiral–spiral pairs are more likely to be enhanced compared to the spirals in mixed spiral–elliptical pairs. The suppression (or

zero enhancement) of star formation in the disks in the mixed pairs may be caused by the extended X-ray halos (i.e., hot gas) of an early-type companion of a spiral galaxy and prevent the spiral from forming stars, or there is no inflow of cold gas from the early-type companion (Park & Choi 2009; Hwang et al. 2010). Furthermore, SFR enhancement seems to be correlated with the properties of the orbit of the two interacting galaxies, as shown by the simulations of Sparre & Springel (2016), in which high-density gas preferentially appears in head-on mergers with very high collision velocities. This scenario is difficult to test directly by observation due to the ambiguity, even when detailed models can be constructed, in a system's geometry and orbital parameters. Finally, SFR enhancement is also found to correlate with H I fraction (e.g., Scudder et al. 2015). Since the galaxies in pairs used in this work are not restricted to any specific merger property, the scatter in each r_p bin is somewhat expected. We should note that part of this scatter is also due to the fact that the r_p is not a direct measure of the merging sequence because galaxies in pairs would merge after several encounters, and their orbital geometry is complicated. This presumably also introduces some extra scatter in the relation.

Turning to the gas properties, panels (b) and (c) present the change of ΔM_{H_2} and Δf_{gas} with r_p, respectively. All symbols are as defined for panel (a). Here ΔM_{H_2} and Δf_{gas} versus r_p show very similar behavior to ΔSFR, and ΔM_{H_2} and Δf_{gas} gradually increase from $\sim$0 dex at 70 kpc to $\sim$0.7 and 0.6 dex, respectively, at <10 kpc. In particular, the figures show that almost all close pairs ($r_p \leqslant 25$ kpc) appear to have M_{H_2} and f_{gas} enhancements.

Here we compare our results of Δf_{gas} with other studies in which the offset of gas properties is also calculated. The 11 galaxies in pairs in Violino et al. (2018) have an r_p range of 16–30 kpc. The median offset M_{H_2} and f_{gas} of their galaxies in pairs are 0.34 and 0.40 dex, respectively. For our galaxies in pairs in the same r_p range, the median ΔM_{H_2} and Δf_{gas} are 0.49 and 0.46, respectively, slightly higher than that of Violino et al. (2018). It may simply be due to low number statistics. The degree of the f_{gas} enhancement of our galaxies in pairs at short r_p ($\sim$0.6 dex) is consistent with that of the sample of post-mergers (M. Sargent et al. 2018, in preparation).

The dependence of ΔSFE on r_p is different from that of ΔSFR, ΔM_{H_2}, and Δf_{gas}. Statistically, SFE enhancements only occur at the smallest pair separations ($r_p < 20$ kpc) by $\sim$0.5 dex. In other words, although overall, the ΔSFE shows zero enhancement (Figure 4(h)), there is a systematic offset for the smallest r_p galaxies. The scatter of ΔSFE is large at large r_p. We will discuss the possible contribution of the large scatter later in the discussion section (Section 4.2).

The statistical significances of the correlations are assessed by calculating the Kendall's τ correlation coefficients. The correlation coefficients are -0.33, -0.29, and -0.29 for r_p versus ΔSFR, ΔM_{H_2}, and Δf_{gas}, respectively. If we restrict the analysis to galaxies with $r_p < 30$ kpc, where the offset values appear to rise more rapidly with decreasing r_p, the correlation coefficients become -0.40, -0.30, and -0.31 for ΔSFR, ΔM_{H_2}, and Δf_{gas}, respectively. The correlation coefficients suggest that there are only marginal anticorrelations between ΔSFR, ΔM_{H_2}, and Δf_{gas} and the pair separation, possibly due to the large scatter at a fixed r_p. The absence of a correlation between r_p and ΔSFE is also suggested by the correlation coefficient of -0.10 across all galaxies in pairs. The
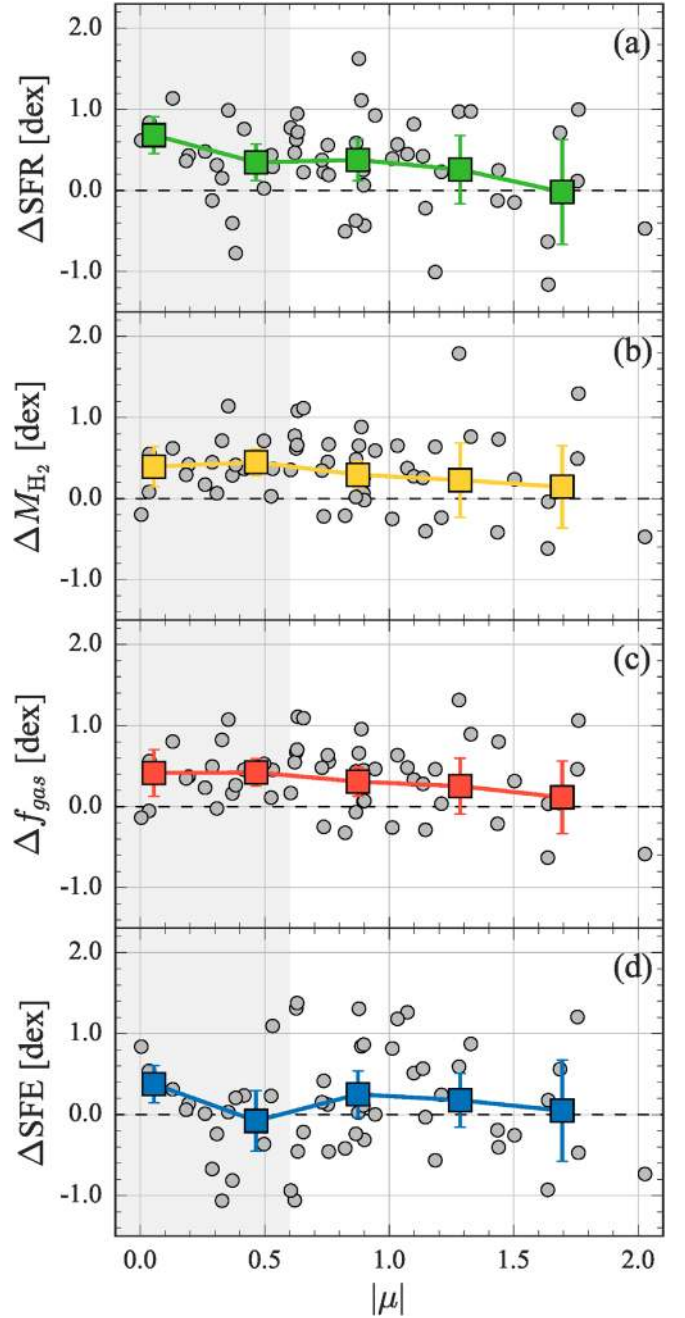
Figure 9. Offset properties as a function of the absolute value of stellar mass ratio $|\mu|$ of the galaxies in pairs. The major-merger regime ($|\mu| < 0.6$) is highlighted in gray. The individual galaxies in pairs are shown with gray circles, and the means are in colored symbols. The ΔSFR, ΔM_{H_2}, and Δf_{gas} exhibit a trend with mass ratio of the two galaxies in a pair. We find no apparent dependence between the mass ratio and ΔSFE. Any SFE enhancement is only significant in the equal-mass pairs ($|\mu| \approx 0$).

correlation coefficient of r_p and ΔSFE becomes -0.22 for galaxies with $r_p < 30$ kpc.

3.4. ΔSFR, Δf_{gas}, and ΔSFE as a Function of Mass Ratio

Our sample covers about a two orders of magnitude mass ratio and includes both primary and secondary galaxies. Since the number of secondary galaxies is considerably smaller than the primary galaxies (11 versus 45), thus not allowing us to compare between these two populations, in this section, we

consider the absolute value of mass ratio $|\mu|$. Figure 9(a) presents ΔSFR as a function of $|\mu|$. The major-merger regime ($|\mu| < 0.6$) is shown in gray. The individual galaxies in pairs are shown with gray circles, and the means are in colored symbols.

The mean ΔSFRs are progressively higher for smaller $|\mu|$ values. Most, but not all, major mergers in our sample show SFR enhancement. As suggested by simulations, a major merger is not inevitably accompanied by significant SFR enhancement, depending on the geometry of the collisions (Cox et al. 2008; Moreno et al. 2015; Sparre & Springel 2016). This may explain why some of the major mergers show low ΔSFR.

The ΔM_{H_2} and Δf_{gas} exhibit a similar trend as ΔSFR in Figures 9(b) and (c), increasing from large to low-mass ratio. On the other hand, the ΔSFE trend with mass ratio is not as strong as for other properties. There is no significant difference in ΔSFE across $|\mu|$. Statistically, SFE enhancements only occur in the equal-mass pairs ($|\mu| \approx 0$) by ~0.4 dex.

We also quantify the degree of correlations between the offset properties and $|\mu|$ using the Kendall's τ correlation coefficient. The correlation coefficients are -0.25, -0.18, -0.20, and -0.001 for ΔSFR, ΔM_{H_2}, Δf_{gas}, and ΔSFE, respectively, indicating marginal trends for equal-mass pairs to have higher ΔSFR, ΔM_{H_2}, and Δf_{gas} but not ΔSFE.

4. Discussion

4.1. Are the Enhanced ΔM_{H_2} and Δf_{gas} Real?

While several studies have suggested the enhancement of ΔM_{H_2} and Δf_{gas} in galaxies in pairs (e.g., Combes et al. 1994; Casasola et al. 2004; Violino et al. 2018), it remains unclear from where this mass excess originates. We first check whether the enhanced ΔM_{H_2} and Δf_{gas} are real.

The enhanced ΔM_{H_2} and Δf_{gas} could be the contamination from the CO emission of the companions. We check the possible contamination by comparing the projected separation between two galaxies in a pair and the beam size (radius). For galaxies with $r_p > 30$ kpc, the distance to the companion is well beyond the beam area, with a median distance of $8\times$ the beam radius. For galaxies with $11 < r_p < 30$ kpc, companions are located at $1.5–10\times$ the beam radius away from the pointing of the CO observations; the median distance is $3\times$ the beam radius. For the close pairs with <11 kpc, the beam areas cover a part of the disk of their companions. In one of the cases, the nucleus of the companion falls within the beam area. Consequently, there must be a nonnegligible contribution of CO emission from the companions in these measurements. However, it is unlikely to be the sole cause of the enhanced ΔM_{H_2} and Δf_{gas}, as the offsets are considerably larger than a factor of 2 (or 0.3 dex), and the positive offsets are seen in galaxies beyond the separation for contamination. Moreover, Δf_{gas} enhancement is seen in post-mergers by ~0.6 dex (M. Sargent et al. 2018, in preparation), where there is only one galaxy in the beam. Therefore, an additional mechanism must be involved in boosting the amount of molecular gas. Nonetheless, we conservatively quote an overestimation (underestimation) of 0.3 dex, corresponding to ~2 times, for the derived ΔM_{H_2} and Δf_{gas} (ΔSFE), assuming a situation consisting of a major merger where both galaxies fall within the beam area.

The observed enhanced ΔM_{H_2} and Δf_{gas} could partially be a selection effect toward high-SFR objects (and thus likely molecular gas-rich), since some of the pair sample (PI program, JINGLE, and JINGLE Pilot) are selected based reaching a minimum S/N level of 4 in an on-source time shorter than 250 minutes that is estimated on the basis of observed SFR and the empirical SFR–M_{H_2} relation (Section 2). We cannot fully rule out the possibility that with deeper data, we would detect more galaxies in pairs with ΔM_{H_2} and Δf_{gas} comparable to that of the control sample. For example, a far-infrared ($\propto$SFR) selection of galaxies in the Coma cluster prevented Casoli et al. (1991) from finding molecular gas–deficient galaxies in clusters, while H_2-deficient galaxies are now widely found when other selection criteria are used, such as stellar mass (e.g., Boselli et al. 2014).

In order to consider such an effect, we additionally match the galaxies in pairs and controls in SFR with an initial tolerance of 0.1 dex and a step of 0.05 dex. In carrying out this test with the extra matching parameter, we find that it is difficult to have at least five control galaxies for each pair, due to the limited number of pool galaxies; thus, the minimal number of control galaxies is instead set to three. Moreover, we were unable to identify control galaxies for some galaxies in pairs with high sSFR; these objects are excluded from the analysis here. The results are presented in Figures 10(a)–(d).

With SFR as one of the matching parameters (Figure 10(a)), the enhancements of ΔM_{H_2} and Δf_{gas} are still present in galaxies in pairs, although with smaller values. The distributions of ΔM_{H_2} and Δf_{gas} when additionally matched in SFR are presented in Figures 10(b) and (c). The median ΔM_{H_2} and Δf_{gas} become 0.19 and 0.11 dex (~55% and 30%), respectively. This reduction of the difference in molecular gas content between galaxies in pairs and controls when they additionally matched in SFR is also found by Violino et al. (2018). However, we note that the median values here should be treated as lower limits, since the galaxies in pairs with high sSFR are not considered, and these galaxies potentially have large ΔM_{H_2} and Δf_{gas}.

After matching in SFR, SFE seems to be suppressed in galaxies in pairs. The median ΔSFE is -0.20 dex (Figure 10(d)). This is not unexpected, since SFE is SFR (matched with controls) divided by M_{H_2} (enhanced) by definition.

In addition, we also perform another test to examine the potential bias induced by different selection criteria for galaxies in pairs (see Section 2), that is, only including galaxies from xCOLD GASS (without matching in SFR). In this case, the selection of a control sample uses exactly the same criteria as for galaxies in pairs. This would also remove any uncertainty in the conversion between CO(2–1) and CO(1–0) intensities. The results are shown in Figures 10(e)–(h) (specifically, these plots are made with the same data values that generated Figures 4(e)–(h), but only galaxies in pairs from xCOLD GASS are shown). It is evident that the distributions of ΔSFR, ΔM_{H_2}, and Δf_{gas} still peak at higher values with respect to the controls when only the xCOLD GASS galaxies in pairs are considered. The median offset values are ~0.3 dex for ΔSFR, ΔM_{H_2}, and Δf_{gas} and ~0.1 dex for ΔSFE.

Overall, we argue that the contamination from companions and selection effects are not the main causes of the enhanced ΔM_{H_2} and Δf_{gas}.
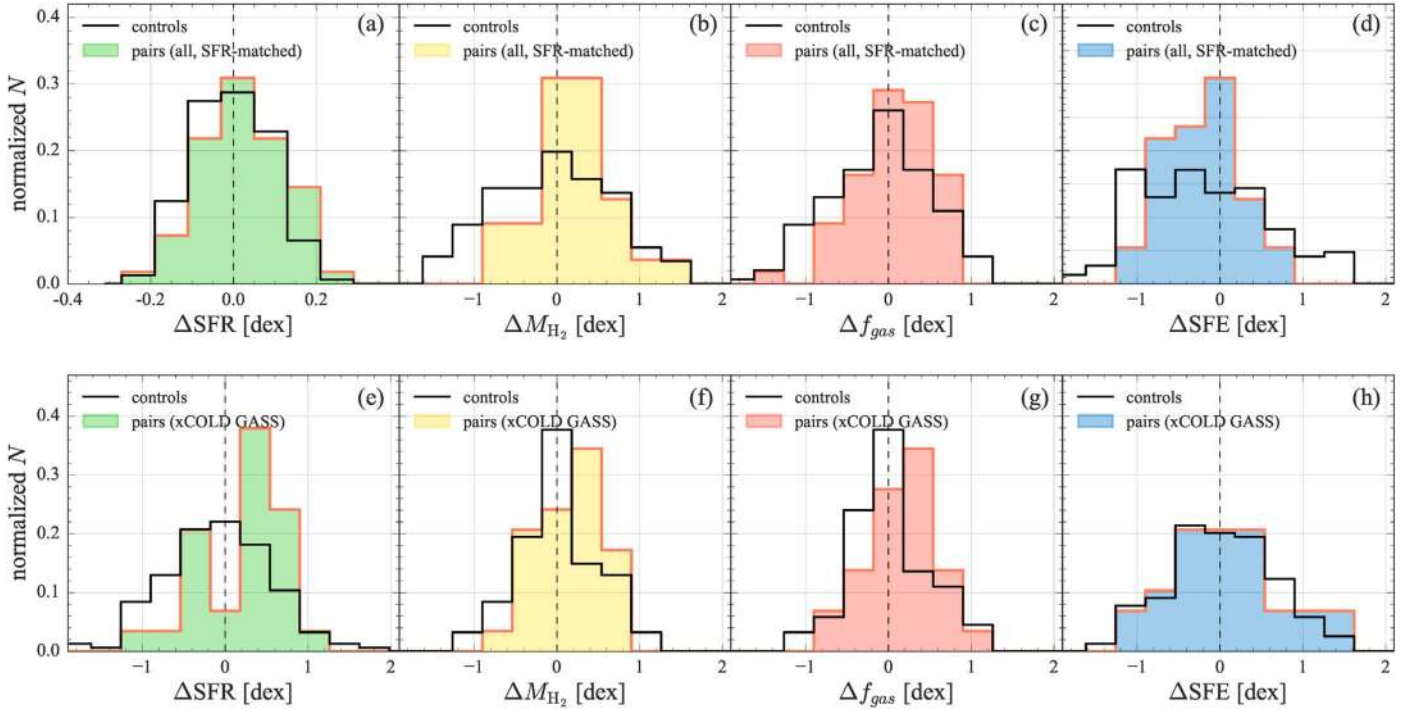
Figure 10. (a)–(d) Normalized distribution of ΔSFR, $\Delta M_{\mathrm{H_2}}$, Δf_{gas}, and ΔSFE. The plot is similar to that of Figures 4(e)–(h), but we additionally match the galaxies and control sample in SFR. Therefore, the values along the x-axis in panel (a) are considerably smaller than those in the other panels. Galaxies in pairs with high sSFR are not considered here (see text for details) due to the lack of suitable controls. With SFR as one of the matching parameters, the enhancements of $\Delta M_{\mathrm{H_2}}$ and Δf_{gas} are still present in galaxies in pairs. The SFE seems to be suppressed in galaxies in pairs after matching in SFR. This is because SFE is SFR divided by $M_{\mathrm{H_2}}$ by definition. (e)–(h) The plots are made using the data values that generated Figures 4(e)–(h) (without matching in SFR), but only galaxies in pairs from xCOLD GASS are shown. Since the control galaxies are drawn from xCOLD GASS as well, any potential bias induced by different selection criteria for galaxies in pairs (Section 2) and any uncertainty in the conversion from CO(2–1) to CO(1–0) intensities are removed. It is evident that the distributions of ΔSFR, $\Delta M_{\mathrm{H_2}}$, and Δf_{gas} still peak at higher values with respect to the controls when only the xCOLD GASS galaxies in pairs are considered.

4.2. What Drives the Gas Reservoir Enhancement?

The main results of this work are that (1) there is a clear enhancement in the gas reservoir ($M_{\mathrm{H_2}}$ and f_{gas}) in galaxies in pairs (Section 3.2); (2) $M_{\mathrm{H_2}}$ and f_{gas} increase by a similar degree to SFR, while the SFE is compatible with not being enhanced (Section 3.2); (3) the correlation with ΔSFR is stronger for $\Delta M_{\mathrm{H_2}}$ and Δf_{gas} than ΔSFE (Section 3.2); and (4) the dependences of $\Delta M_{\mathrm{H_2}}$ and Δf_{gas} on merger configurations are similar to that of ΔSFR, with ΔSFR, $\Delta M_{\mathrm{H_2}}$, and Δf_{gas} increasing with decreasing r_p and $|\mu|$, whereas ΔSFE is not exhibiting any trend, with only close pairs ($r_p < 10$ kpc) and equal-mass systems ($|\mu| \approx 0$) being affected significantly (Section 3.3).

The results of our work are in broad agreement with several previous studies. Combes et al. (1994) also found a correlation of SFR and molecular gas mass (both are in raw values) with r_p. At the same time, they found that the SFE shows no evidence for a correlation with r_p and is only enhanced in galaxies displaying the strongest distortion, presumably analogous to the objects with the smallest r_p in our sample. A similar conclusion is reached by Casasola et al. (2004) with several hundred galaxies in pairs with CO data from the literature. They found that galaxies in pairs have more molecular gas than normal galaxies; however, the gas does not seem to be more efficient in forming stars.

Some studies propose opposite results, favoring SFE as the prime driver of interaction-induced star formation. Solomon & Sage (1988) found that only strong interactions show enhanced SFE. Sofue et al. (1993) found an elevated SFE in Arp peculiar

galaxies. The fact that SFE is enhanced in our close pairs is in agreement with these studies, since these are strongly interacting galaxies and Arp peculiar galaxies that, by definition, must be close to each other. However, these studies find no difference in total gas mass between isolated galaxies and galaxies in pairs, which leads to the conclusion that SFE is the determining factor in triggering star formation. It is not clear where this discrepancy stems from. The possible sources of the discrepancy could be the choice of α_{CO} and the definition of the isolated (control) galaxy sample. In fact, many widely separated spectroscopic pairs show no obvious distortion in their morphology but do show enhancement of SFR, $M_{\mathrm{H_2}}$, and f_{gas}. This emphasizes the importance of large spectroscopic data sets for identifying pairs and controls.

The physical origin of the enhanced $M_{\mathrm{H_2}}$ and f_{gas} is still unclear. One possible reason for the enhancement is an efficient transition from atomic to molecular gas by external pressure, as suggested by Kaneko et al. (2017). The cause of the external pressure can be the widespread shocks produced by interaction prevailing throughout a galaxy and cloud–cloud collisions in colliding regions (Icke 1985; Barnes 2004; Braine et al. 2004; Roche et al. 2015). Such an acceleration of the H I-to-H_2 transition occurs even in the early stages of interaction (Kaneko et al. 2017). Moreover, Braine & Combes (1993) proposed a scenario in which the gravitational torque induced by galaxy interaction provokes the infall of diffuse ionized halo gas inward. The ionized gas progressively turns into atomic gas because cooling becomes more efficient with increasing density. Merger simulations by Moreno et al. (2018) indeed find that ionized gas is depleted during the interaction phase

probed by galaxy pairs. At a certain radius, because of the high density and cold temperature, the gas enters the molecular phase, causing growth of the H_2 mass. The scenario is supported by cosmological hydrodynamical simulations (Moster et al. 2011) and binary merger simulations (Moreno et al. 2018). Moreover, the origin of the enhanced M_{H_2} and f_{gas} might be somewhat analogous to what is being encountered by galaxies in clusters. Mok et al. (2016, 2017) showed that Virgo cluster galaxies have a significantly higher H_2-to-$H\,I$ ratio than the group sample. They interpret it as being a result of the various forms of interaction between galaxies that lead to gas flowing toward the center of host galaxies and the creation of H_2. However, Ellison et al. (2015, 2018) showed that there is no decrease in $H\,I$ in late-stage galaxy mergers. It could still be possible that the $H\,I$ reservoir fuels the H_2 but that the interplay with other phases also plays a role and replenishes the $H\,I$ (e.g., Moreno et al. 2018).

The impact of galaxy interactions is less evident for SFE (except for the closest and equal-mass pairs) when considering the globally averaged properties. The comparable integrated SFE of local early-stage pairs and isolated systems is in line with theoretical predictions. The simulations of Renaud et al. (2014) found that, on a galaxy-wide scale, approaching pairs are forming stars with similar efficiency as local spirals because the gravitational interaction and inflow are too weak to significantly increase the gas density. As many of our galaxies in pairs are in an early-stage interaction with their companion (i.e., two separated galaxies), the normal SFE of our galaxies in pairs is not surprising. Besides, we cannot exclude the possibility that galaxy interactions affect SFE at a much smaller scale than f_{gas}, such as the nuclear region, collision front, or particular side (e.g., leading or trailing) with respect to the interaction, and thus the variation in SFE is averaged out in a galaxy-wide study. The small-scale variation in SFE may also contribute to the large scatter of SFE among the galaxies in pairs (Figure 8), as the measured global SFE would depend on the observed area of a galaxy and various projection effects.

As the merger proceeds, the nuclear gas surface density of gas gets boosted by gravitational torques and inflows, making the gas more efficient at converting gas into stars (Mihos & Hernquist 1996; Renaud et al. 2014; Sparre & Springel 2016; Bustamante et al. 2018), and the system moves to its starburst phase. In agreement with the simulations, the SFE appears to be enhanced in our close pairs undergoing a strong interaction. However, it is worth cautioning that while nuclear starbursts are frequent among mergers (in both simulations and observations), observationally, there is a significant fraction of systems in which interaction-triggered star formation is taking place outside the nuclear region (García-Marín et al. 2009; Cortijo-Ferrero et al. 2017; H.-A. Pan et al. 2018, in preparation; Thorp et al. 2019). Simulations based on the standard star formation model, i.e., in which the local SFR is related to the local gas density, often fail to reproduce this large-scale star formation (e.g., Barnes 2004; Chien & Barnes 2010; Bournaud et al. 2011) and underestimate the SFR in regions where gas exhibits large velocity dispersions (e.g., Mihos et al. 1993; Barnes 2004; Chien & Barnes 2010; Bournaud et al. 2011). Shock-induced and clustered star formation have been suggested to better account for the large-scale star formation in many interacting galaxies (e.g., Jog & Solomon 1992; Barnes 2004; Saitoh et al. 2009; Teyssier et al. 2010; Powell et al. 2013).

Finally, we should note that, as pointed out by Violino et al. (2018), the decrease of SFR-matched ΔM_{H_2} and Δf_{gas} implies that internal mechanisms in isolated galaxies can have an effect similar to that caused by galaxy interactions. Mechanisms such as a bar instability could be a potential driver to accelerate atomic-to-molecular gas transitions (Masters et al. 2012) and promote star formation (Martinet & Friedli 1997; Ellison et al. 2011; Carles et al. 2016; Kim et al. 2017) in isolated galaxies. However, the formation of bars may be closely tied with galaxy interactions (Noguchi 1987; Lang et al. 2014; Łokas et al. 2016).

4.3. SFR–M_{H_2} Relation

The SFR (or SFR surface density) is observed to correlate with M_{H_2} (or M_{H_2} surface density) with a power-law index of $N \approx 1$–2 (Kennicutt & Evans 2012). Figure 11 illustrates the integrated SFR–M_{H_2} relation of our galaxies in pairs (red circles) and controls (gray squares). The two populations largely overlap on the SFR–M_{H_2} plane, as also observed for the nearby galaxies in pairs in Violino et al. (2018; see their Figure 8). This is a consequence of the similar SFE between galaxies in pairs and controls (at all but the smallest separations). The linear least-squares fits ($\log(SFR) = N \times \log M_{H_2} + b$) yield a slope of $\sim N \approx 1.11 \pm 0.15$ for both galaxies in pairs and controls.

In order to better understand the role of galaxy interactions on star formation and connect the different galaxy populations, we compare our galaxies with 23 local isolated normal galaxies (green diamonds), 110 local galaxies in the Virgo cluster and nearby clouds (yellow pentagons), 19 local isolated (U)LIRGs (blue triangles), 49 local (U)LIRG mergers (orange hexagons), and 26 high-z (U)LIRGs (purple thin diamonds).

Local isolated normal galaxies and (U)LIRGs. The local isolated normal galaxies and (U)LIRGs are taken from Gao & Solomon (2004). An infrared luminosity of $10^{11}\,L_\odot$ is used to distinguish between normal galaxies and (U)LIRGs. Only galaxies that were observed in $^{12}CO(1\text{–}0)$ with the IRAM 30 m and NRAO 12 m telescopes are used in this work. Galaxies in Gao & Solomon (2004) that have been classified as galaxy pairs and group galaxies from the NASA/IPAC Extragalactic Database (NED)[34] were removed (see Table 1 in Gao & Solomon 2004); however, we cannot completely rule out the possibility of these (U)LIRGs being mergers. Most of the normal isolated objects are NGC galaxies, while the isolated (U)LIRGs are IRAS and Markarian galaxies.

Local galaxies in the Virgo cluster and nearby clouds. The local galaxies in dense environments, including the Virgo cluster and nearby clouds, are taken from the *Herschel* Reference Sample[35] (HRS; Boselli et al. 2010). The nearby clouds are Leo, Ursa Major and Ursa Major Southern Spur, Crater, Coma I, Canes Venatici Spur and Canes Venatici-Camelopardalis, and Virgo-Libra Clouds. Galaxies are removed from the analysis if they have been identified as early type by NED or are located at the Virgo outskirts. The molecular gas data in $^{12}CO(1\text{–}0)$ for the HRS are either obtained at the Kitt Peak 12 m telescope or compiled from the literature (Boselli et al. 2014).

Local (U)LIRG mergers. The measurements of local (U)LIRG mergers are compiled from Gao & Solomon (1999). The

---

[34] https://ned.ipac.caltech.edu/
[35] https://hedam.lam.fr/HRS/
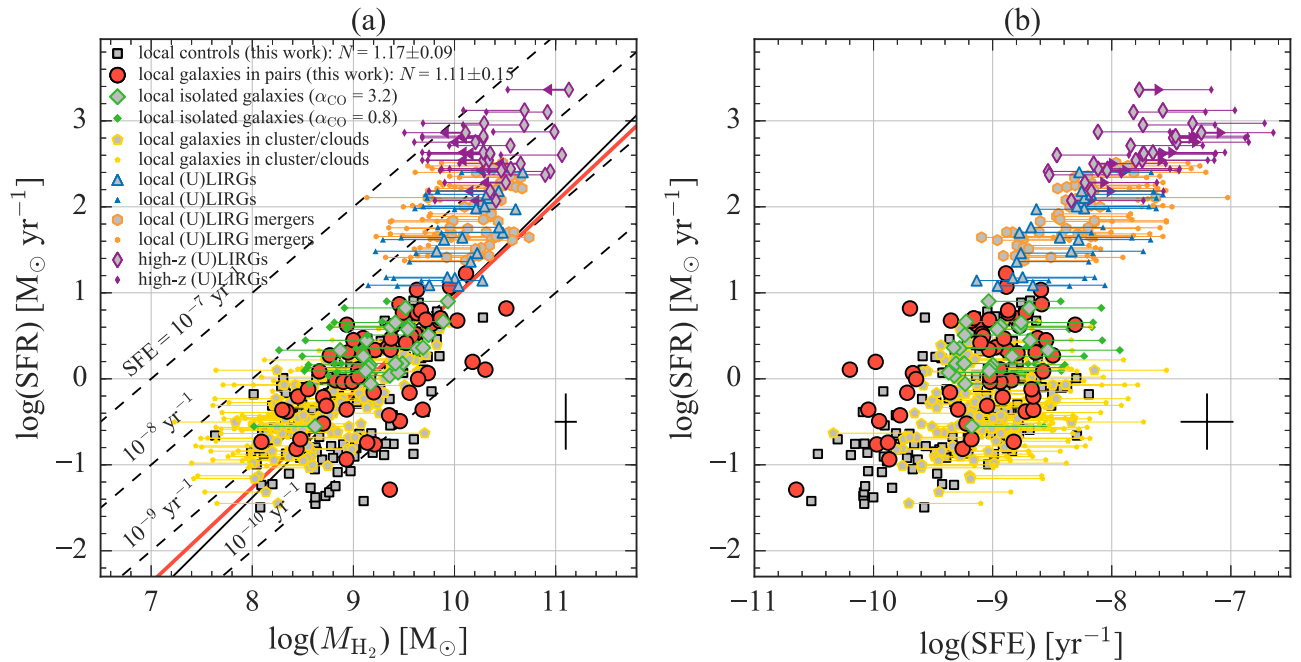
Figure 11. The SFR plotted as a function of (a) mass and (b) SFE of molecular gas. Our galaxies in pairs and the pool of controls are shown as red circles and gray squares, respectively. Red and black solid lines give the best-fitting linear relation for our galaxies in pairs and controls, respectively. The values of the best-fitting power-law index are given in the plot. Literature data have been included for comparison. The local normal isolated galaxies (green diamonds) and (U)LIRGs (blue triangles) are taken from Gao & Solomon (2004). Galaxies in the Virgo cluster and nearby clouds are taken from the HSR (yellow pentagons; Boselli et al. 2010). Orange hexagons show local (U)LIRG mergers from Gao & Solomon (1999). Purple thin diamonds show high-z (U)LIRGs from Combes et al. (2013). Due to the lack of metallicity and M_* measurements to calculate the physically motivated α_{CO}, we apply two values of α_{CO}, 3.2 (large symbols) and 0.8 (small symbols), for all galaxies compiled from the literature (see text for details). The two symbols of a given galaxy are connected with a horizontal line, indicating the most plausible range of M_{H_2} for the galaxy. In the cases where the line is not detected, the upper limits of L_{CO} and M_{H_2} are computed at 3σ. These galaxies are indicated by a horizontal arrow (all of them are high-z (U)LIRGs). The SFRs of the local isolated galaxies and local and high-z (U)LIRGs are calculated using L_{IR} calibrated by Kennicutt (1998b). The SFRs of the HSR galaxies are determined by the mean values of different SFR estimates using Hα, 24 μm, FUV, and radio (Boselli et al. 2015). The figure shows that the gap between our galaxies and high-z (U)LIRGs on the SFR–M_{H_2} plane (the bimodal star formation mode) can be bridged by local (U)LIRGs. Moreover, the high SFR of high-z (U)LIRGs is due to not only an enhancement of the molecular gas reservoir but also the SFE of the molecular gas.

observations were made with the IRAM 30 m, NRAO 12 m, and SEST 15 m telescopes at ^{12}CO(1–0). The (U)LIRG mergers are IRAS, Markarian, and Arp galaxies.

High-z (U)LIRG. The high-z ($0.2 < z < 1.0$) (U)LIRGs are taken from Combes et al. (2013). Data of multiple CO transitions were taken, but in Figure 11, we only use the galaxies with ^{12}CO(2–1) observed with the IRAM 30 m telescope, which is the lowest transition in Combes et al. (2013). Combes et al. (2013) assumed a line ratio of 1 between the ^{12}CO(2–1) and ^{12}CO(1–0), as expected for warm, optically thick, and thermally excited gas in starburst objects. About half of these high-z (U)LIRGs are interacting or merging systems, while the remaining objects appear unperturbed. Because of the increasing gas fraction with redshift, high-z galaxies can easily be (U)LIRGs without violent interactions (e.g., Davé et al. 2010; Kartaltepe et al. 2012). Moreover, the high fraction of unperturbed high-z (U)LIRGs is in part due to the low resolution and sensitivity when imaging high-z galaxies. In those cases where the line is not detected, the upper limits of L_{CO} and M_{H_2} are computed at 3σ.

Due to the lack of metallicity and M_* measurements necessary to calculate the physically motivated α_{CO}, we apply two values for α_{CO}, 3.2 and 0.8, for all galaxies compiled from the literature. The higher α_{CO} is the median value of our galaxies in pairs and controls; the lower α_{CO} is the commonly adopted conversion factor for (U)LIRGs and distant galaxies (e.g., Solomon et al. 1997; Downes & Solomon 1998; Daddi et al. 2010; Combes et al. 2013). Both results are plotted in

Figure 11 with large symbols for $\alpha_{CO} = 3.2$ and small symbols for $\alpha_{CO} = 0.8$. The two symbols of a given galaxy are connected with a horizontal line, indicating the most plausible range of M_{H_2} for the galaxy. The range of M_{H_2} of nondetected galaxies is also computed based on the upper limits of L_{CO}. These galaxies are indicated by a horizontal arrow.

The SFRs of the local isolated galaxies and local and high-z (U)LIRGs are calculated using infrared luminosity (L_{IR}; Kennicutt 1998b),

$$\frac{\text{SFR}}{(M_\odot \ \text{yr}^{-1})} = 4.5 \times 10^{-44} \frac{L_{IR}}{(\text{erg s}^{-1})}, \qquad (7)$$

assuming a Salpeter IMF. The SFRs of the HSR galaxies are determined by the mean values of different SFR estimates using Hα, 24 μm, FUV, and radio, along with a Salpeter IMF (Boselli et al. 2015). It is necessary to multiply these Salpeter SFRs by 0.625 to transform from Salpeter IMF to Kroupa IMF.

With $\alpha_{CO} = 3.2$, the local isolated galaxies and galaxies in the Virgo cluster and nearby clouds populate the same regime in SFR–M_{H_2} space as our galaxies in isolation and in pairs. The SFE of local galaxies could increase to up to $\sim 10^{-8}$ yr^{-1} if the lower conversion factor is used. The choice of the lower conversion factor for local galaxies might not be realistic (e.g., Sandstrom et al. 2013; Cormier et al. 2018), but it characterizes a potential upper limit of local SFE.

No matter which α_{CO} is used, the SFE increases from local non-(U)LIRG galaxies, to local (U)LIRGs and (U)LIRG mergers, to high-z (U)LIRGs. The change of SFE across the

galaxy populations can be better seen in Figure 11(b), where we plot the SFR versus SFE of the gas. In other words, the high SFR of high-z (U)LIRGs is due to not only an enhancement of the molecular gas reservoir but also the enhanced SFE of the gas.

The different SFEs of high-z and local star-forming galaxies have previously been considered as "bimodal" (Daddi et al. 2010; Genzel et al. 2010). In other words, local star-forming galaxies and high-z starburst galaxies are two distinct populations. However, Figure 11 shows that the gap in the relation that extends from our local galaxies to the high-z (U) LIRGs is filled by local (U)LIRGs, confirming the finding of Saintonge et al. (2011).

Some of our galaxies in pairs, both major and minor mergers, may become infrared-bright galaxies between the first passage and final coalescence during which star formation is dramatically boosted (e.g., Di Matteo et al. 2008; Kartaltepe et al. 2012; Renaud et al. 2014; in fact, a few of our galaxies in pairs have SFRs comparable to those of local (U)LIRGs, as seen in Figure 11). Carpineti et al. (2015) found that around 65% of local LIRGs are minor mergers (see also Ellison et al. 2013, and their Figure 10). However, minor mergers typically do not induce enough gas into the nuclear region to generate ULIRG-level luminosities. In the local universe, the majority of ULIRGs are triggered by almost equal-mass, gas-rich systems in advanced merger stages (Dasyra et al. 2006; Hwang et al. 2010; Carpineti et al. 2015).

4.4. Caveats of This Work

One caveat of the total gas mass determination is the fact that traditionally, the SDSS only probes the central 3″. However, metallicity gradients have been observed in galaxies with a typical gradient of ~-0.05 dex kpc^{-1} (Pilyugin et al. 2014; Ho et al. 2015; Belfiore et al. 2017). The influence of using nuclear metallicity instead of globally averaged metallicity to calculate α_{CO} is presumably stronger for isolated galaxies than galaxies in pairs due to interaction-induced radial mixing of gas, which flattens the metallicity profiles (Ellison et al. 2008; Michel-Dansac et al. 2008; Kewley et al. 2010; Scudder et al. 2012; Thorp et al. 2019).

Another caveat to the total gas mass determination is the assumption of $^{12}CO(2-1)$ to $^{12}CO(1-0)$ ratio (R_{21}) for the sample observed in the $J = 2 \rightarrow 1$ transition. In this work, we adopted an R_{21} of 0.8, which is an average value of the spatially resolved R_{21} of nearby galaxies (Leroy et al. 2009) and corresponds to optically thick gas with an excitation temperature of ~ 10 K. However, R_{21} varies from region to region in the Milky Way and nearby galaxies: ~ 0.6–1.0 in the spiral arms and galactic centers (star-forming molecular clouds) and <0.6 in the interarm regions (dormant molecular clouds; e.g., Leroy et al. 2009; Koda et al. 2012; Pan et al. 2015). If a higher value of R_{21} is adopted ($R_{21} \approx 0.9$–1), the M_{H_2}, as well as the ΔM_{H_2} and Δf_{gas} with respect to the controls (which are observed at $J = 1 \rightarrow 0$), would decrease. However, such a high value of R_{21} is only observed in the nuclear regions; given that R_{21} decreases with increasing galactocentric radius (Leroy et al. 2009), the true value of the globally averaged R_{21} should be lower than that. It is also unlikely that our galaxies in pairs are dominated by dormant clouds, since they are actively forming stars; therefore, a globally averaged $R_{21} < 0.6$ is not possible. Accordingly, we argue that our results should be only minimally affected by the assumption for R_{21}. Nonetheless, it is important to note that a variation of the

$^{12}CO(3-2)$-to-$^{12}CO(1-0)$ ratio as a function of the merger sequence of (U)LIRGs has been reported (Leech et al. 2010; Michiyama et al. 2016).

5. Summary

We investigate the effect of galaxy interactions on global molecular gas properties by studying a sample of 58 galaxies in pairs (Section 2.1) and 154 control galaxies (Section 2.2). Molecular gas properties are determined from observations with the JCMT 15 m, PMO 14 m, and CSO 10 m telescopes and supplemented with data from the xCOLD GASS and JINGLE surveys at $^{12}CO(2-1)$ and $^{12}CO(1-0)$. The main conclusions are summarized below.

1. The median values of the SFR, M_{H_2}, and f_{gas} distributions of the full pairs sample are higher compared with those of the full control (nonmerger) sample. The differences between the control sample and galaxies in pairs are confirmed statistically by the K-S test. On the other hand, the SFE distribution of galaxies in pairs is statistically indistinguishable from that of the control sample (Section 3.1 and Figure 4).

2. We compute offsets in M_{H_2}, f_{gas}, and SFR on a galaxy-by-galaxy basis by identifying controls that are matched in redshift, stellar mass, and effective size. All gas property offsets (ΔM_{H_2}, Δf_{gas}, and ΔSFE) increase with ΔSFR, implying that both the available gas reservoir and the SFE of the gas are expected to influence SFR. However, the correlations are stronger for ΔM_{H_2} and Δf_{gas} than for ΔSFE in terms of correlation coefficients (Section 3.2 and Figures 4 and 6).

3. The ΔSFR, ΔM_{H_2}, and Δf_{gas} all increase with decreasing pair separation (r_p) over the range from ~ 70 to 10 kpc. However, any SFE enhancement is only significant at the smallest pair separations ($r_p < 20$ kpc; Section 3.3 and Figure 8).

4. The ΔSFR, ΔM_{H_2}, and Δf_{gas} also exhibit a trend with stellar mass ratio of the two galaxies in a pair. Statistically, higher enhancements are found in pairs with smaller mass ratio. We find no apparent trend between the mass ratio and ΔSFE; it seems that statistically, SFE enhancements only occur in equal-mass pairs ($|\mu| \approx 0$; Section 3.4 and Figure 9).

5. If we additionally match the galaxies in pairs in SFR with controls, the gas mass and fraction are still enhanced in galaxies in pairs with respect to the controls, although by a smaller factor (Section 4.1 and Figure 4.1).

6. Our local galaxies in pairs and controls are largely overlapping on the SFR–M_{H_2} relation as a result of their comparable SFE ($=$SFR$/M_{H_2}$). The SFE of our galaxies is an order of magnitude lower than that in the high-z (U) LIRGs. The gap between our galaxies and high-z (U)LIRGs on the SFR–M_{H_2} plane can be bridged by local (U)LIRGs. Moreover, the high SFR of high-z (U)LIRGs is due to not only an enhancement of molecular gas reservoir but also the SFE of the gas (Section 4.3 and Figure 11).

All of the above, taken together, lead to the conclusion that galaxy interactions modify the total molecular gas mass, molecular gas mass fraction, and SFR of a galaxy, although the strength of the effect is dependent on merger properties.

Here we have only accounted for integrated properties. The next step of this work is to probe the spatially resolved star

formation and molecular gas properties. A direct comparison of spatially resolved ΔSFR and molecular gas properties will extend our understanding of the star formation process in galaxy pairs, e.g., where the enhanced M_{H_2}, f_{gas}, and SFR are actually to be found. ALMA observations of MaNGA galaxies will be ideal for carrying out such an analysis.

ORCID iDs

Hsi-An Pan ⓘ https://orcid.org/0000-0002-1370-6964
Lihwai Lin ⓘ https://orcid.org/0000-0001-7218-7407
Bau-Ching Hsieh ⓘ https://orcid.org/0000-0001-5615-4904
Yang Gao ⓘ https://orcid.org/0000-0002-6316-1632
Jorge Barrera-Ballesteros ⓘ https://orcid.org/0000-0003-2405-7258
Amélie Saintonge ⓘ https://orcid.org/0000-0003-4357-3450
Christine D. Wilson ⓘ https://orcid.org/0000-0001-5817-0991
Ho Seong Hwang ⓘ https://orcid.org/0000-0003-3428-7612
Luis C. Ho ⓘ https://orcid.org/0000-0001-6947-5846
Elias Brinks ⓘ https://orcid.org/0000-0002-7758-9699
Angus Mok ⓘ https://orcid.org/0000-0001-7413-7534
Aeree Chung ⓘ https://orcid.org/0000-0003-1440-8552
Harriet Parsons ⓘ https://orcid.org/0000-0002-6327-3423
Martin Bureau ⓘ https://orcid.org/0000-0003-4980-1012
Mark T. Sargent ⓘ https://orcid.org/0000-0003-1033-9684
Eun Jung Chung ⓘ https://orcid.org/0000-0003-0014-1527
Tie Liu ⓘ https://orcid.org/0000-0002-5286-2564

References

Accurso, G., Saintonge, A., Catinella, B., et al. 2017, MNRAS, 470, 4750
Arimoto, N., Sofue, Y., & Tsujimoto, T. 1996, PASJ, 48, 275
Baldwin, J. A., Phillips, M. M., & Terlevich, R. 1981, PASP, 93, 5
Barnes, J. E. 2004, MNRAS, 350, 798
Barnes, J. E., & Hernquist, L. 1996, ApJ, 471, 115
Belfiore, F., Maiolino, R., Maraston, C., et al. 2016, MNRAS, 461, 3111
Belfiore, F., Maiolino, R., Tremonti, C., et al. 2017, MNRAS, 469, 151
Blanton, M. R., Bershady, M. A., Abolfathi, B., et al. 2017, AJ, 154, 28
Bolatto, A. D., Wolfire, M., & Leroy, A. K. 2013, ARA&A, 51, 207

Borne, K. D., Bushouse, H., Colina, L., et al. 1999, Ap&SS, 266, 137
Boselli, A., Cortese, L., Boquien, M., et al. 2014, A&A, 564, A67
Boselli, A., Eales, S., Cortese, L., et al. 2010, PASP, 122, 261
Boselli, A., Fossati, M., Gavazzi, G., et al. 2015, A&A, 579, A102
Bothwell, M. S., Kennicutt, R. C., & Lee, J. C. 2009, MNRAS, 400, 154
Bothwell, M. S., Maiolino, R., Cicone, C., Peng, Y., & Wagg, J. 2016, A&A, 595, A48
Bournaud, F., Chapon, D., Teyssier, R., et al. 2011, ApJ, 730, 4
Braine, J., & Combes, F. 1992, A&A, 264, 433
Braine, J., & Combes, F. 1993, A&A, 269, 7
Braine, J., Lisenfeld, U., Duc, P.-A., et al. 2004, A&A, 418, 419
Brinchmann, J., Charlot, S., White, S. D. M., et al. 2004, MNRAS, 351, 1151
Bruzual, G., & Charlot, S. 2003, MNRAS, 344, 1000
Bundy, K., Bershady, M. A., Law, D. R., et al. 2015, ApJ, 798, 7
Bustamante, S., Sparre, M., Springel, V., & Grand, R. J. J. 2018, MNRAS, 479, 3381
Cao, C., Xu, C. K., Domingue, D., et al. 2016, ApJS, 222, 16
Carles, C., Martel, H., Ellison, S. L., & Kawata, D. 2016, MNRAS, 463, 1074
Carpineti, A., Kaviraj, S., Hyde, A. K., et al. 2015, A&A, 577, A119
Casasola, V., Bettoni, D., & Galletta, G. 2004, A&A, 422, 941
Casoli, F., Boisse, P., Combes, F., & Dupraz, C. 1991, A&A, 249, 359
Chang, Y.-Y., van der Wel, A., da Cunha, E., & Rix, H.-W. 2015, ApJS, 219, 8
Charlot, S., Kauffmann, G., Longhetti, M., et al. 2002, MNRAS, 330, 876
Charlot, S., & Longhetti, M. 2001, MNRAS, 323, 887
Chien, L.-H., & Barnes, J. E. 2010, MNRAS, 407, 43
Cid Fernandes, R., Pérez, E., García Benito, R., et al. 2013, A&A, 557, A86
Combes, F., García-Burillo, S., Braine, J., et al. 2013, A&A, 550, A41
Combes, F., Prugniel, P., Rampazzo, R., & Sulentic, J. W. 1994, A&A, 281, 725
Cormier, D., Bigiel, F., Jiménez-Donaire, M. J., et al. 2018, MNRAS, 475, 3909
Cortijo-Ferrero, C., González Delgado, R. M., Pérez, E., et al. 2017, MNRAS, 467, 3898
Cox, T. J., Jonsson, P., Somerville, R. S., Primack, J. R., & Dekel, A. 2008, MNRAS, 384, 386
Currie, M. J., Berry, D. S., Jenness, T., et al. 2014, in ASP Conf. Ser. 485, Astronomical Data Analysis Software and Systems XXIII, ed. N. Manset & P. Forshay (San Francisco, CA: ASP), 391
Daddi, E., Elbaz, D., Walter, F., et al. 2010, ApJL, 714, L118
Darg, D. W., Kaviraj, S., Lintott, C. J., et al. 2010a, MNRAS, 401, 1552
Darg, D. W., Kaviraj, S., Lintott, C. J., et al. 2010b, MNRAS, 401, 1043
Dasyra, K. M., Tacconi, L. J., Davies, R. I., et al. 2006, ApJ, 638, 745
Davé, R., Finlator, K., Oppenheimer, B. D., et al. 2010, MNRAS, 404, 1355
Davies, L. J. M., Robotham, A. S. G., Driver, S. P., et al. 2015, MNRAS, 452, 616
Di Matteo, P., Bournaud, F., Martig, M., et al. 2008, A&A, 492, 31
Di Matteo, P., Combes, F., Melchior, A.-L., & Semelin, B. 2007, A&A, 468, 61
Donoso, E., Yan, L., Tsai, C., et al. 2012, ApJ, 748, 80
Downes, D., & Solomon, P. M. 1998, ApJ, 507, 615
Ellison, S. L., Catinella, B., & Cortese, L. 2018, MNRAS, 478, 3447
Ellison, S. L., Fertig, D., Rosenberg, J. L., et al. 2015, MNRAS, 448, 221
Ellison, S. L., Mendel, J. T., Patton, D. R., & Scudder, J. M. 2013, MNRAS, 435, 3627
Ellison, S. L., Nair, P., Patton, D. R., et al. 2011, MNRAS, 416, 2182
Ellison, S. L., Patton, D. R., Simard, L., & McConnachie, A. W. 2008, AJ, 135, 1877
Gao, Y., & Solomon, P. M. 1999, ApJL, 512, L99
Gao, Y., & Solomon, P. M. 2004, ApJS, 152, 63
García-Marín, M., Colina, L., Arribas, S., & Monreal-Ibero, A. 2009, A&A, 505, 1319
Genzel, R., Tacconi, L. J., Gracia-Carpio, J., et al. 2010, MNRAS, 407, 2091
Gunn, J. E., Siegmund, W. A., Mannery, E. J., et al. 2006, AJ, 131, 2332
Ho, I.-T., Kudritzki, R.-P., Kewley, L. J., et al. 2015, MNRAS, 448, 2030
Hsieh, B. C., Lin, L., Lin, J. H., et al. 2017, ApJL, 851, L24
Hwang, H. S., Elbaz, D., Dickinson, M., et al. 2011, A&A, 535, A60
Hwang, H. S., Elbaz, D., Lee, J. C., et al. 2010, A&A, 522, A33
Icke, V. 1985, A&A, 144, 115
Jiang, X.-J., Wang, Z., Gu, Q., Wang, J., & Zhang, Z.-Y. 2015, ApJ, 799, 92
Jog, C. J., & Solomon, P. M. 1992, ApJ, 387, 152
Kaneko, H., Kuno, N., Iono, D., et al. 2017, PASJ, 69, 66
Kartaltepe, J. S., Dickinson, M., Alexander, D. M., et al. 2012, ApJ, 757, 23
Kauffmann, G., Heckman, T. M., Tremonti, C., et al. 2003b, MNRAS, 346, 1055
Kauffmann, G., Heckman, T. M., White, S. D. M., et al. 2003a, MNRAS, 341, 33
Kennicutt, R. C., & Evans, N. J. 2012, ARA&A, 50, 531

Kennicutt, R. C., Jr. 1998a, ApJ, 498, 541
Kennicutt, R. C., Jr. 1998b, ARA&A, 36, 189
Kewley, L. J., Dopita, M. A., Sutherland, R. S., Heisler, C. A., & Trevena, J. 2001, ApJ, 556, 121
Kewley, L. J., Rupke, D., Zahid, H. J., Geller, M. J., & Barton, E. J. 2010, ApJL, 721, L48
Kim, E., Hwang, H. S., Chung, H., et al. 2017, ApJ, 845, 93
Knapen, J. H., Cisternas, M., & Querejeta, M. 2015, MNRAS, 454, 1742
Koda, J., Scoville, N., Hasegawa, T., et al. 2012, ApJ, 761, 41
Koyama, S., Koyama, Y., Yamashita, T., et al. 2017, ApJ, 847, 137
Kroupa, P. 2001, MNRAS, 322, 231
Lambas, D. G., Tissera, P. B., Alonso, M. S., & Coldwell, G. 2003, MNRAS, 346, 1189
Lang, M., Holley-Bockelmann, K., & Sinha, M. 2014, ApJL, 790, L33
Larson, R. B., & Tinsley, B. M. 1978, ApJ, 219, 46
Lee, J. C., Hwang, H. S., & Ko, J. 2013, ApJ, 774, 62
Leech, I., Isaak, K. G., Papadopoulos, P. P., Gao, Y., & Davis, G. R. 2010, MNRAS, 406, 1364
Leroy, A. K., Bolatto, A., Gordon, K., et al. 2011, ApJ, 737, 12
Leroy, A. K., Walter, F., Bigiel, F., et al. 2009, AJ, 137, 4670
Leroy, A. K., Walter, F., Brinks, E., et al. 2008, AJ, 136, 2782
Lin, L., Koo, D. C., Weiner, B. J., et al. 2007, ApJL, 660, L51
Lin, L., Koo, D. C., Willmer, C. N. A., et al. 2004, ApJL, 617, L9
Łokas, E. L., Ebrová, I., del Pino, A., et al. 2016, ApJ, 826, 227
Mannucci, F., Cresci, G., Maiolino, R., Marconi, A., & Gnerucci, A. 2010, MNRAS, 408, 2115
Martig, M., & Bournaud, F. 2008, MNRAS, 385, L38
Martinet, L., & Friedli, D. 1997, A&A, 323, 363
Masters, K. L., Nichol, R. C., Haynes, M. P., et al. 2012, MNRAS, 424, 2180
Mendel, J. T., Simard, L., Palmer, M., Ellison, S. L., & Patton, D. R. 2014, ApJS, 210, 3
Michel-Dansac, L., Lambas, D. G., Alonso, M. S., & Tissera, P. 2008, MNRAS, 386, L82
Michiyama, T., Iono, D., Nakanishi, K., et al. 2016, PASJ, 68, 96
Mihos, J. C., Bothun, G. D., & Richstone, D. O. 1993, ApJ, 418, 82
Mihos, J. C., & Hernquist, L. 1996, ApJ, 464, 641
Mok, A., Wilson, C. D., Golding, J., et al. 2016, MNRAS, 456, 4384
Mok, A., Wilson, C. D., Knapen, J. H., et al. 2017, MNRAS, 467, 4282
Moreno, J., Torrey, P., Ellison, S. L., et al. 2015, MNRAS, 448, 1107
Moreno, J., Torrey, P., Ellison, S. L., et al. 2018, MNRAS, submitted
Moster, B. P., Macciò, A. V., Somerville, R. S., Naab, T., & Cox, T. J. 2011, MNRAS, 415, 3750
Narayanan, D., Bothwell, M., & Davé, R. 2012, MNRAS, 426, 1178
Noguchi, M. 1987, MNRAS, 228, 635
Pan, H.-A., Kuno, N., Koda, J., et al. 2015, ApJ, 815, 59
Park, C., & Choi, Y.-Y. 2009, ApJ, 691, 1828
Patton, D. R., Pritchet, C. J., Carlberg, R. G., et al. 2002, ApJ, 565, 208
Patton, D. R., Torrey, P., Ellison, S. L., Mendel, J. T., & Scudder, J. M. 2013, MNRAS, 433, L59
Pettini, M., & Pagel, B. E. J. 2004, MNRAS, 348, L59
Pilyugin, L. S., Grebel, E. K., & Kniazev, A. Y. 2014, AJ, 147, 131
Powell, L. C., Bournaud, F., Chapon, D., & Teyssier, R. 2013, MNRAS, 434, 1028
Renaud, F., Bournaud, F., Kraljic, K., & Duc, P.-A. 2014, MNRAS, 442, L33
Roche, N., Humphrey, A., Gomes, J. M., et al. 2015, MNRAS, 453, 2349
Saintonge, A., Catinella, B., Tacconi, L. J., et al. 2017, ApJS, 233, 22
Saintonge, A., Kauffmann, G., Wang, J., et al. 2011, MNRAS, 415, 61
Saintonge, A., Tacconi, L. J., Fabello, S., et al. 2012, ApJ, 758, 73
Saintonge, A., Wilson, C. D., Xiao, T., et al. 2018, MNRAS, 481, 3497
Saitoh, T. R., Daisaka, H., Kokubo, E., et al. 2009, PASJ, 61, 481
Salim, S., Rich, R. M., Charlot, S., et al. 2007, ApJS, 173, 267
Sanders, D. B., Soifer, B. T., Elias, J. H., et al. 1988, ApJ, 325, 74
Sandstrom, K. M., Leroy, A. K., Walter, F., et al. 2013, ApJ, 777, 5
Sargent, M. T., Daddi, E., Béthermin, M., et al. 2014, ApJ, 793, 19
Scudder, J. M., Ellison, S. L., Momjian, E., et al. 2015, MNRAS, 449, 3719
Scudder, J. M., Ellison, S. L., Torrey, P., Patton, D. R., & Mendel, J. T. 2012, MNRAS, 426, 549
Sofue, Y., Wakamatsu, K.-I., Taniguchi, Y., & Nakai, N. 1993, PASJ, 45, 43
Solomon, P. M., Downes, D., Radford, S. J. E., & Barrett, J. W. 1997, ApJ, 478, 144
Solomon, P. M., & Sage, L. J. 1988, ApJ, 334, 613
Sparre, M., & Springel, V. 2016, MNRAS, 462, 2418
Springel, V., & Hernquist, L. 2005, ApJL, 622, L9

19

Taylor, E. N., Hopkins, A. M., Baldry, I. K., et al. 2011, MNRAS, 418, 1587
Teyssier, R., Chapon, D., & Bournaud, F. 2010, ApJL, 720, L149
Thorp, M. D., Ellison, S. L., Simard, L., Sánchez, S. F., & Antonio, B. 2019, MNRAS, doi:10.1093/mnrasl/sly185
Tremonti, C. A., Heckman, T. M., Kauffmann, G., et al. 2004, ApJ, 613, 898
Violino, G., Ellison, S. L., Sargent, M., et al. 2018, MNRAS, 476, 2591

Wake, D. A., Bundy, K., Diamond-Stanic, A. M., et al. 2017, AJ, 154, 86
Whitaker, K. E., van Dokkum, P. G., Brammer, G., & Franx, M. 2012, ApJL, 754, L29
Wong, K. C., Blanton, M. R., Burles, S. M., et al. 2011, ApJ, 728, 119
Xu, C. K., Domingue, D., Cheng, Y.-W., et al. 2010, ApJ, 713, 330
Xu, C. K., Shupe, D. L., Béthermin, M., et al. 2012, ApJ, 760, 72